Title

Thermo-physical phase field model of laser powder melting additive manufacturing of layered stainless steel structures

Author

Roberts, Collin

Publication Date

2023

Peer reviewed|Thesis/dissertation

UNIVERSITY OF CALIFORNIA

Los Angeles

Thermo-physical phase field model of laser powder melting additive manufacturing of layered stainless steel structures

A dissertation submitted in partial satisfaction
of the requirements for the degree
Doctor of Philosophy in Materials Science and Engineering

by

Collin Sebastian Roberts

2023

ABSTRACT OF THE DISSERTATION

Thermo-physical phase field model of laser powder melting additive manufacturing of layered stainless steel structures

by

Collin Sebastian Roberts
Doctor of Philosophy in Materials Science and Engineering
University of California, Los Angeles, 2023
Professor Jaime Marian, Chair

The high temperature gradients present in additive manufacturing (AM) processes tend to produce microstructures in metallic materials that are not seen in other manufacturing processes. Large columnar grains oriented parallel to the build direction in AM materials are an important feature to quantify based on their ability to affect the mechanical properties of the output material. In this work we present a thermo-physical phase field model that combines an implicit solution to the heat equation in two dimensions while simultaneously modeling the explicit heterogeneous nucleation and growth of solidifying material in the active build layer. After construction of a simulated bulk material, finite-element analyses can be performed to determine the expected mechanical properties. Given the varied parameter space present in AM processes, an efficient method is presented to utilize machine learning methods to predict the effect of various microstructural features on the output mechanical properties of yield strength and post-yield hardening rate.

The dissertation of Collin Sebastian Roberts is approved.

Sergey Prikhodko

Yinmin Wang

Xiaochun Li

Amartya S. Banerjee

Jaime Marian, Committee Chair

University of California, Los Angeles

2023

Immeasurable thanks go to my wife, family, and cat for
their relentless support in my quest for a head full of knowledge.

TABLE OF CONTENTS

LIST OF FIGURES

LIST OF TABLES

ACKNOWLEDGMENTS

I must thank Dr. Jaime Marian and Dr. Sergey Prikhodko for their mentorship during my graduate career. I am grateful for the knowledge they have shared, as well as the time they have offered to ensure my academic success.

I must also thank co-authors and collaborators for their part in our combined research efforts. In Chapter 3, Jaime Marian and I acknowledge the efforts of Cameron McElfresh, Sicong He, and Sergey Prikhodko, as well as support from the National Science Foundation under Grant DMR-1611342, the US Department of Energy's Office of Fusion Energy Sciences, Project DE-SC0012774, and NATO 's Science for Peace and Security, Project G5787. Computer time allocations at UCLA's IDRE Hoffman2 supercomputer are also acknowledged.

VITA

2018	B.S. (Engineering Physics), The Ohio State University.
2019–2022	Graduate Research Assistant, Materials Science and Engineering Department, UCLA
2019–2022	Teaching Assistant, Life Sciences, Physics, and MSE Departments, UCLA. Taught sections of Physics 1B, 5A, 5C, Life Science 30A, and MSE 143A, 111L.
2022	Associate Engineer–Post Grad, SpaceX
2023	Materials Engineer II, SpaceX

PUBLICATIONS AND PRESENTATIONS

Roberts, C., Lannutti, R., Munoz, G. (2018). *Nanofiber-based sensors and apparatus for oxygen measurement* (U.S. Patent Application No. 16,009,824). U.S. Patent and Trademark Office

McElfresh, C., Roberts, C., He, S., Prikhodko, S., & Marian, J. (2022). Using machine-learning to understand complex microstructural effects on the mechanical behavior of Ti-6Al-4V alloys. *Computational Materials Science. 208.* 111267.

Roberts, C. (2022). Using machine-learning to understand complex microstructural effects on the mechanical behavior of Ti-6Al-4V alloys. Presented at TMS 2022, Anaheim, CA

Roberts, C. (2023). Phase-Field Simulations of Additively Manufactured Microstructures for High-Entropy Alloys. Presented at USACM Workshop on Data-Driven and Computational Modeling of Materials Across Scales, Los Angeles, CA

Markovsky, P.E., Savvakin, D.G., Stasyuk, O.O., Mecklenburg, M., Pozuelo, M., Roberts, C., Ellison, V., & Prikhodko, S.V. (2023). Significant Hardening Effect of High-Temperature Aging of Alloy Ti-6Al-4V Composite Reinforced with TiC. *Materials & Design*. 112208.

Roberts, C., Marian, J. (2023). Thermo-physical phase field model of laser powder melting additive manufacturing of layered stainless steel structures. (*To be determined*).

CHAPTER 1

Introduction

Selective laser melting (SLM) is an additive manufacturing (AM) technique characterized by layer-by-layer melting of a powdered metal deposited onto a substrate plate that is selectively fused to the previous layer with a high-power laser [1]. This process allows for the creation of more geometrically complex parts with less material at faster prototyping cycles than traditional metal manufacturing techniques involving subtractive manufacturing, forging, or casting [2]. Additionally, parts made with AM methods can exhibit improved mechanical properties such as yield strength when compared to reference components made with traditional methods [3, 4]. However, the high temperature gradients present in SLM processes have marked effects on the resultant microstructure of the component made. Notable among these microstructural features is the formation of large columnar grains oriented parallel to the build direction. Naturally, then, it can be inferred that parts produced with SLM may show greater anisotropy in mechanical properties than cast alloys with a higher proportion of equiaxed grains. Analyzing the presence and quantifying the properties of these columnar grains would lead to better understanding of bulk-scale component performance while also informing the AM processing parameters needed to achieve the desired mechanical output of a given component [5, 6].

SLM-AM processing can be slow and costly and is characterized by a large parameter space. Moreover, slight variations in the parameters involved can have a strong impact on microstructural outcomes [7]. As such, modeling and simulation has emerged as a useful tool to efficiently parse through the many degrees of freedom controlling SLM-AM and

identify those with the highest impact [8–13]. Models that take a physics-based approach to couple printing parameters (e.g., laser power, scan speed, hatch spacing, layer height) to solidification characteristics of the deposited material (e.g., specific heat, density, enthalpy, diffusion rates) can be utilized to predict features of the resulting microstructure, and in some cases, predict the mechanical behavior of the as-built components. However, high-fidelity modeling of the additive manufacturing process has proven difficult due to the influence of multi-scale and multi-physics phenomena such as nucleation and solidification, powder packing and multi-pass effects, fluid flow and Marangoni effects, martensitic transformations, as well as the contribution from defects such as key-holing, lack of fusion, vaporization, solute segregation, and hot cracking. As such, various simulation techniques have been employed to capture different mechanisms of the fabrication process, including phase field modeling (PFM) [14–17], kinetic Monte Carlo (kMC) [18, 19], the finite element method (FEM) [12, 20–23], computational fluid dynamics (CFD) [11, 24], and cellular automata (CA) [25–29].

While AM modeling is eminently a three-dimensional process, 3D-approaches are computationally intensive, which limits the time and length scales of what is computationally achievable [30]. However, it is not clear how 2D simulations can reliably approximate three-dimensional settings. Only in cases where columnar growth is the operative physical mechanism are 2D models suited to simulate AM processes [31]. Indeed, columnar structures during SLM-AM are often seen in the direction of heat extraction, i.e., when heat flow is orthogonal to the scan direction [32]. Columnar grains can also appear in laser powder-bed melting processing when solidified grains are seen to grow along crystal directions dictated by the underlying substrates or support layer [33, 34]. In such conditions, two-dimensional models that use the z direction as a boundary condition, both in terms of heat flow and crystallographic biasing, may be appropriate to simulate SLM-AM processing.

One potential application for SLM manufacturing is titanium alloys which are widely used in aerospace, biomedical, transportation, and military applications due to their specific high strength and fracture toughness, corrosion resistance, and high-temperature properties.

In particular, Ti-6Al-4V is one of the most popular titanium alloys due to the increased strength achieved with the stabilization of the body-centered cubic (BCC) β phase. The interplay between the hexagonal close-packed (HCP) α phase and the β phase is the primary factor dictating the strength of titanium alloys. Though the β phase is thermodynamically unfavorable below 890°C in pure titanium [35, 36], metastable dual-phase titanium alloys are possible through the addition of a mixture of beta-stabilizers (such as silicon and vanadium) and alpha-stabilizers (such as aluminum or oxygen). One of the primary advantages of α/β alloys is that they are heat treatable. Heat treating is vital to relieve residual stresses, remove machining history, or tune the microstructure for the ability of mass-manufacturing the material, making α/β alloys a continued area of interest for manufacturing and material science alike.

A number of previous studies have shown that thermo-mechanical processing of α/β Ti alloys can achieve a particular microstructure-performance combination for various applications [37]. Dual-phase titanium can exist in a number of microstructures including equiaxed, duplex, lamellar, intergranular, and lath [38, 39]. In addition, there is interest in better understanding graded or layered microstructures that may be ideal for lightweight or directionally-dependent high strength applications [40]. The advantageous properties of titanium alloys make them ideal candidates for many high-performance applications. However, the parametric space including all property-dependent microstructural features (grain size, phase fraction, orientation, texture, grain geometry, reinforcement particle size and distribution, solutes etc.) makes alloy design a multifactorial process of combinatorial proportions. As such, mapping the effect of one parameter –or of sets of different parameters– to a specific microstructural property or mechanical response through experimentation alone is thus impractical. For this reason, computational modeling and data analysis can become essential tools to establish direct correlations and narrow down the parametric space in search for improved alloys via micro- and macrostructural design.

Traditional computational modeling methods, such as crystal plasticity (CP), are ideal

counterparts to experimental methods in order to study the various features associated with the deformation behavior and mechanical coupling between the β and α phases. Indeed, different variants of the CP method have been applied in recent times to modeling the deformation of dual-phase titanium alloys [41–45]. However, while useful to study specific aspects of microstructural evolution during alloy deformation, these tools alone cannot capture the complexities associated with the broad parametric space potentially influencing the material response. Capturing complex correlations between sets of variables requires using additional tools of statistical nature.

Advances in computing power and data availability have, among other things, propelled the widespread use of machine learning (ML) as an additional means of capturing meaning from data. The materials science modeling community has benefited from the use of machine learning techniques in studies utilizing density functional theory [46], dislocation dynamics [47], molecular dynamics [48], crystal plasticity [49], and others [50–52]. The relatively low cost to entry into the domain of machine learning makes it an ideal resource to complement data-heavy research processes. Moreover, machine learning techniques are ideal to apply when constructing a predictor for mechanical behavior because (i) there are often many features that affect a material's mechanical response, and (ii) the property-behavior relationship of the features tends to be non-linear. Many machine learning models excel at capturing non-linear behavior and have been successfully applied to build regressors that predict mechanical behavior for a wide range of materials including steels [53, 54], composites [55], and metallic glasses [56–58]. It should be emphasized that while there are constitutive equations that are used to model the mechanical behavior of alloys, the arbitrary extension of these expressions to include more (possibly non-linear) variables is not trivial [59, 60]. In this way, the use of ML as opposed to traditional constitutive expressions also decreases the rigor of expanding the model to include more feature variables as the data becomes available.

In Chapter 2 we develop a full PFM for simulating layer-by-layer, selective laser-melting additive manufacturing of 316L stainless steels. Our model starts from an existing substrate

which acts both as heat sink and as a seed for grain orientation, known as *oriented growth*. We solve the full thermo-physical system defined by a phase evolution equation of the Allen-Cahn type coupled to the heat diffusion equation, using a heterogeneous nucleation and growth model.

In Chapter 3 we employ several machine learning regression techniques in an exercise to develop predictive models for the strength and hardening rate of α/β dual-phase polycrystals. Our microstructure simulator is a crystal plasticity approach based on the work by Admal *et al.*[61] adapted to polycrystals with alternating BCC/HCP structures representative of dual-phase Ti alloys. The CP model is used to generate large data sets relating specific inputs to objective outputs, and ML regression techniques are then applied to assign importances and extract correlations.

CHAPTER 2

Simulating additively manufactured microstructures

2.1 Simulation setup

The basic process to be simulated involves a laser with a finite spot width scanning an area using an alternating sweep pattern such that every point in the simulation domain is at least once directly under the laser beam. We assume that the laser always encounters a thin layer of metal powder upstream. This layer is then molten underneath the laser spot and re-solidifies dynamically following heat dissipation away from the melt pool. Powders are always deposited on an existing substrate created by previous sweeps of the laser beam. Solidification of the molten powders takes place subjected to the microstructural constraints imposed by the underlying substrate (to be explained below). With each sweep, the total specimen thickness grows by some amount assumed to be sufficiently thin to guarantee columnar growth [31]. For this reason, our model can be considered as a '2.5-dimensional' approach in which 3D information can be extracted from two-dimensional simulations provided that reasonable validity limits are acknowledged.

2.1.1 Laser spot dynamics

The motion of the laser spot follows the pattern illustrated schematically in Figure 2.1 for every layer of the simulation. Other studies show the effects of laser scan pattern on defect formation and microstructural evolution [62], but for simplicity this work utilizes a single laser track pattern. The laser has a spot diameter of d_{spot} moving at a velocity v_{spot}.

Table 2.1: Laser parameters for AM algorithm iterations.

Parameter	Value	Units
T_{spot}	2595	K
v_{spot}	300, 400, 500	$\text{mm} \cdot \text{s}^{-1}$
d_{spot}	0.3, 0.4, 0.5	mm
W_{hatch}	$1.5r_{\text{spot}}$, $1.6r_{\text{spot}}$, $1.7r_{\text{spot}}$	mm
$\dot{P}$	230	W

Each successive pass is spaced by a distance W_{hatch} separating the centers of the laser spot. Table 2.1 gives the values considered in this work for d_{spot}, W_{hatch}, and v_{spot}. $\dot{P}$ is the laser power, which will be defined below. Simulations take place on a two-dimensional domain characterized by a square mesh with step size equal to $\Delta x = \Delta y$. The distance moved by the laser is normalized by the time step Δt and the mesh spacing Δx so the spot moves an equal number of mesh spaces per iteration. After crossing the top edge of the simulation space, the laser is held in a *cool-down* position outside the mesh, allowing the microstructure to solidify in the wake of the hot spot. The laser moves in the positive x-direction in sequential vertical sweeps separated by a full hatch distance. This is repeated until the simulation domain is swept in its entirety. After a full coverage of the computational domain, the laser heat source is removed from the simulation and the microstructure is allowed to cool to room temperature.

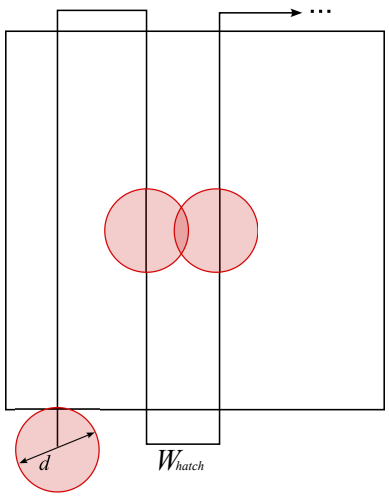

Figure 2.1: Schematic representation of laser path in the simulation domain.

2.1.2 Layer-by-layer deposition

Laser heating always occurs over a pre-existing solid substrate with a special texture determined by the AM process. The initial microstructure (i.e., at $t = 0$) is a assumed to represent an equiaxed polycrystal (constructed as described in Sec. 2.2.4) with a prescribed average grain size and random texture. During each laser sweep, the metal powders deposited on the substrate melt, after which a nucleation and growth process takes place governed by temperature. As such, suitable simulation methods capable of capturing phase transformation processes are required to model these processes. These are discussed in Sec. 2.2.1.

Solidification of the material via nucleation of new grains in the wake of laser melting is then crystallographically biased by the crystal orientations of the underlying substrate [63–66]. At the same time, existing grains adjacent to the melt pool can grow into it in the same crystal orientation of the parent grain. This leads to two competing crystallographic orientation processes that determine the texture of each successive layer. Next, we provide further details describing the general procedure to implement these two processes.

2.1.2.1 Assignment of crystal orientation by nucleation

When a nucleation event takes place (the nucleation criterion is explained in Sec. 2.2.3) fully inside the melt pool, the nucleated crystal follows the same orientation as the grain immediately beneath it in the underlying substrate. The process is schematically shown in Figure 2.2, and effectively replicates the physical process of (*quasi*)columnar growth. Thus, although the model may be strictly defined for two dimensions, the relation of the physical processes in the active layer (denoted by N) to the underlying substrate ($N-1$) connects the simulation with the third (depth) dimension.

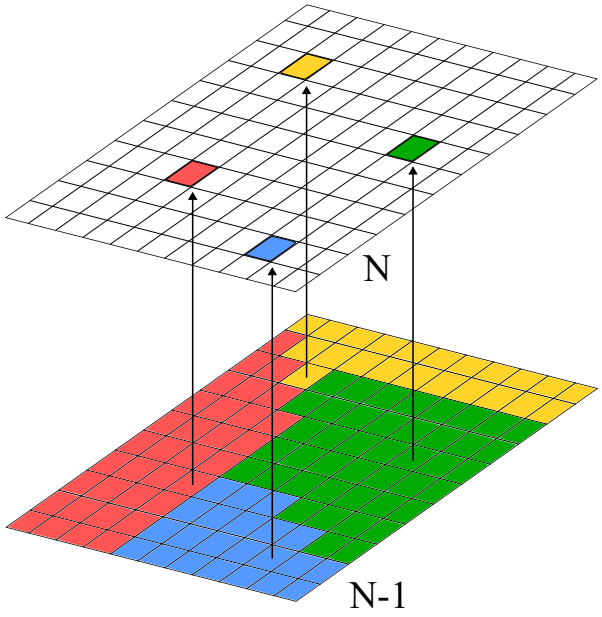

Figure 2.2: Examples of mesh points in layer N that have nucleated and are assigned the value of the same mesh point in layer $N-1$.

2.1.2.2 Assignment by growth

When an existing crystal grain grows into the molten region of the active layer, the mesh elements absorbed by this growth are assigned the same crsytallographic orientation as the solid grain. In the case of triple junctions, i.e., when a grain boundary moves into the

molten region with another solid grain as neighbor, the corresponding mesh elements adopt the orientation of the grain with which it shares the most edges. This is indicated in Figure 2.3, where a mesh element labeled 'X' solidifies with two grains A and B as neighbors. In this case, X is assigned the same crystal orientation as B, as it shares more element edges with it than with A.

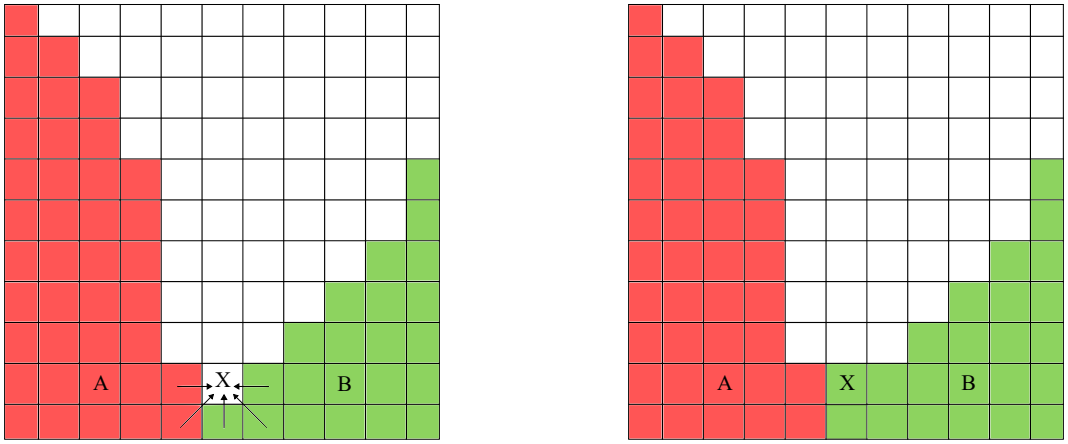

(a) Mesh point X surveys neighbors for grain values.

(b) Mesh point X assumes value of grain B.

Figure 2.3: Schematic representation of grain assignment by growth of surrounding grains.

2.2 Numerical models

2.2.1 Phase field model

The phase field method has been extensively used to model various microstructural phenomena including solidification [67], solid-solid phase transformations [68], fatigue crack growth [2, 69], grain coarsening [30, 70], etc. The model tracks the evolution in time of an order parameter or phase variable, ϕ, whose values represent different phases of the materials or substances involved.

2.2.1.1 Theoretical background

The standard phase-field model is formulated primarily on the basis of appropriately constructing the energy landscape to obtain the correct equilibrium response. The evolution of ϕ follows a steepest descent dynamics, coupled to static or dynamic momentum balance. In general solidification models, the phase-field variable takes two distinct value, $\phi = 0$ to describe the region of amorphous or untransformed material, and $\phi = 1$ to describe the region of crystallized or transformed material. In order to maintain continuity of the associated equations at the interface of the two phases, ϕ changes continuously from $[0, 1]$.

Stability of a given phase is determined by the corresponding Gibbs free energy of the system:

$$G = \int_{\Omega} \left[g_{\text{chem}}(\phi, T, p, ...) + g_{dw}(\phi, T, p, ...) + g_{\text{grad}}(\nabla\phi) \right] d\Omega \tag{2.1}$$

where g_{chem} is the chemical free energy density of a given phase, g_{dw} is the 'double-well' potential energy density, and g_{grad} describes the free energy density present due to the diffuse interfacial regions between the extremes of ϕ. The energy densities used above are defined as follows:

$$\begin{aligned} g_{\text{chem}} &= p(\phi) g_C + (1 - p(\phi))\, g_L = g_L - p(\phi)\Delta g \\ g_{dw} &= W q(\phi) \\ g_{\text{grad}} &= \frac{a^2}{2} \left| \nabla\phi \right|^2 \end{aligned} \tag{2.2}$$

where

$$\begin{aligned} p(\phi) &= \phi^3(6\phi^2 - 15\phi + 10) \\ q(\phi) &= 16\phi^2(1-\phi)^2 \\ \Delta g &= g_C - g_L \\ \delta &= 4\Delta x \\ W &= \frac{6b\gamma_i}{\delta} \\ a &= \sqrt{\frac{3\delta\gamma_i}{b}} \\ b &= 2\tanh^{-1}(1-2\lambda) \end{aligned} \tag{2.3}$$

Here, $p(\phi)$ is an interpolation function, $q(\phi)$ is the double-well potential function, g_L and g_C are the Gibbs free energy densities of the liquid and crystalline phases, respectively, which are taken as constant in this study. W and a describe the height of the energy barrier for the double-well and the gradient energy coefficient, respectively. In the previous equations, γ_i is the interfacial energy between the crystalline and liquid phases [71], δ is the one-dimensional thickness of the interface, and b is a constant used to adjust the thickness of the diffuse interfacial region. The parameters used in this simulation are given in Table 2.2.

The time evolution of the free energy equation is modeled with the Allen-Cahn equation [70, 72]:

$$\frac{\partial\phi}{\partial t} = -M_\phi(T,\phi)\frac{\delta G}{\delta\phi} = M_\phi\left(\frac{\partial p(\phi)}{\partial\phi}\Delta g - W\frac{\partial q(\phi)}{\partial\phi} + a^2\nabla^2\phi\right) \tag{2.4}$$

where M_ϕ is a mobility defined as

$$M_\phi = \frac{\sqrt{2W}}{6a}M(T) \tag{2.5}$$

where $M(T)$ is the physical mobility of the interface, described by an Arrhenius expression:

$$M(T) = M_0\exp\left(-\frac{Q_g}{k_BT}\right) \tag{2.6}$$

where M_0 is a constant mobility prefactor, Q_g is the activation energy for interface motion, and k_B is Boltzman's constant. Several studies cite values for M_0 spanning orders of magnitude, from 10^{-7} to 10^{-5}, even up to $10^{-2}\,\mathrm{m}\cdot\mathrm{s}^{-1}$ [30, 73–76], but in this simulation, the value

Parameter	Value	Units
T_m	1730	K
T_0	300	K
α_S	3.53×10^{-6}	$\mathrm{m}^2 \cdot \mathrm{s}^{-1}$
α_L	3.35×10^{-6}	$\mathrm{m}^2 \cdot \mathrm{s}^{-1}$
h_l	2.70×10^5	$\mathrm{J} \cdot \mathrm{kg}^{-1}$
c	7.27×10^2	$\mathrm{J} \cdot \mathrm{kg}^{-1} \cdot \mathrm{K}^{-1}$
ρ	8000	$\mathrm{kg} \cdot \mathrm{m}^{-3}$
γ_i	0.385	$\mathrm{J} \cdot \mathrm{m}^{-2}$
Q_g	2.19	eV
Q_d	1.40	eV
λ	0.1	–
Δx	5.0×10^{-6}	m
Δt	2.50×10^{-5}	s
M_0	4.0×10^{-3}	$\mathrm{m}^4 \cdot \mathrm{J}^{-1} \cdot \mathrm{s}^{-1}$
θ_c	5.0	deg

Table 2.2: Parameters used in the phase field and temperature simulations.

given in Table 2.2 was chosen and provided stable phase field behavior. The temperature dependence in the grain mobility allows the phase field model to accurately represent grain growth under the temperature gradients present during the AM process, with grains growing preferentially into areas of higher temperature.

2.2.1.2 Phase field explicit solution

The time-discretized solution of the phase field variable is solved with an explicit Euler discretization scheme in time coupled with a central finite difference method in space. Com-

bining eqs. (2.2)-(2.6), and using $\phi^{x,y} \equiv \phi$ for clarity, the discretized form of eq. (2.4) is:

$$\phi_{t+\Delta t} = \phi_t - M_\phi \Delta t \Bigg[30(\phi_t^2 - \phi_t)^2 \Delta g + W(4\phi_t^3 - 6\phi_t^2 + 2\phi_t) - \frac{a^2}{(\Delta x)^2} \left(\phi_t^{x-1,y} + \phi_t^{x+1,y} + \phi_t^{x,y-1} + \phi_t^{x,y+1} - 4\phi_t \right) \Bigg] \quad (2.7)$$

where the superscripts pertaining to the ϕ values account for periodic boundary conditions. This equation is solved with an explicit timestep that adheres to Neumann stability conditions:

$$\Delta t \leq \frac{(\Delta x)^2}{4 M_\phi a^2} \quad (2.8)$$

The chosen time step that adheres to this stability condition is also applied to the implicit solution to the heat equation (discussed in Sec. 2.2.2.1), aligning the temporal scale of the two solvers. In this way, the temperature and phase fields can be solved on the same length scale, eliminating the need for interpolation or other approximation methods.

2.2.2 Temperature field solution

2.2.2.1 Heat diffusion model

In this work, the motion of the laser beam is simulated assuming a time-dependent temperature field, $T(x, y)$, that mirrors the position of the laser spot. $T(x, y)$ for the liquid is obtained by solving the heat equation in conjunction with the Allen-Cahn equation:

$$\frac{\partial T}{\partial t} = \alpha_L \left(\frac{\partial^2 T}{\partial x^2} + \frac{\partial^2 T}{\partial y^2} \right) + \frac{h_l}{c} \frac{\partial \phi}{\partial t} \quad (2.9)$$

where α_L is the thermal diffusivity of the liquid, h_l is the latent heat of fusion, and c is the heat capacity [77–79]. The last term in the r.h.s. of the above equation represents the injection of heat owing to an exothermic phase transformation to the solid phase (i.e., a nucleation event, described below). In this work, the above equation is solved during every iteration after moving the laser spot and fixing the temperature under the spot to a constant value of $T_{\text{spot}} = 1.5 T_m$, where T_m is the melting point, and then solving eq. (2.9) for the

new temperature state at all points. In the solid phase, the above equation simplifies to: $\dot{T} = \alpha_S \nabla^2 T$. In both cases, we assume that the temperature is constant through the entire thickness of the powder layer, i.e., along the depth z-dimension.

The laser power, listed in Table 2.1, can be obtained from the following expression: $\dot{P} = C\rho\alpha_L d_{\text{spot}} \Delta T$, where $\Delta T = T_{\text{spot}} - T_0$.

2.2.2.2 Implicit solution procedure

Equation (2.9) is solved using an implicit Euler discretization scheme in time coupled with a finite difference method in space:

$$\begin{aligned} \frac{T_{t+\Delta t}^{x,y} - T_t^{x,y}}{\Delta t} &= \alpha_\phi \left(\frac{T_{t+\Delta t}^{x-1,y} - 2T_{t+\Delta t}^{x,y} + T_{t+\Delta t}^{x+1,y}}{\Delta x^2} + \frac{T_{t+\Delta t}^{x,y-1} - 2T_{t+\Delta t}^{x,y} + T_{t+\Delta t}^{x,y+1}}{\Delta y^2} \right) + \frac{h_l}{c\Delta t} \left(\phi_{t+\Delta t} - \phi_t \right) \\ T_t^{x,y} &= T_{t+\Delta t}^{x,y} - \frac{\alpha_\phi \Delta t}{(\Delta x)^2} \left(T_{t+\Delta t}^{x-1,y} + T_{t+\Delta t}^{x+1,y} + T_{t+\Delta t}^{x,y-1} + T_{t+\Delta t}^{x,y+1} - 4T_{t+\Delta t}^{x,y} \right) - \frac{h_l}{c} \left(\phi_{t+\Delta t} - \phi_t \right) \end{aligned} \tag{2.10}$$

where α_ϕ denotes the thermal diffusivity of the phase present at a given mesh point. This equation can be written in a matrix form as:

$$\left[\boldsymbol{I} - \frac{\alpha_\phi \Delta t}{(\Delta x)^2} \boldsymbol{\Theta} \right] \boldsymbol{T_{t+\Delta t}} = \boldsymbol{T_t} + \frac{h_l}{c} \left(\boldsymbol{\phi_{t+\Delta t}} - \boldsymbol{\phi_t} \right) \tag{2.11}$$

where $\boldsymbol{\Theta}$ is a (first-nearest neighbor) square mesh connectivity matrix:

$$\Theta_{ij} = \begin{cases} -4 & i = x, j = y \\ 1 & i = x \pm 1, j = y \\ 1 & i = x, j = y \pm 1 \\ 0 & \text{otherwise} \end{cases}$$

This system of equations is computationally solvable with linear algebra methods for the family of cases represented by $\boldsymbol{Ax} = \boldsymbol{b}$. Here, the bracketed matrix on the l.h.s. is a sparse $N \times N$ symmetric positive-definite matrix, allowing for fast computational solutions, even for

large matrices. Here we use a Cholesky factorization to efficiently solve the $\boldsymbol{Ax} = \boldsymbol{b}$ equation for $\boldsymbol{T_{t+\Delta t}}$ based on $\boldsymbol{T_t}$. The system is assumed to be connected to a 300 K temperature reservoir by applying Dirichlet boundary conditions to all points on the boundary of the simulation domain.

An example of the solution for the temperature field in the wake of the moving laser spot is provided in Figure 2.4. The figure shows a color map of the temperature field, the temperature profile along the y-direction for $x = 200\Delta x$, and several Gaussian profiles corresponding to several time instances after the laser spot passed.

2.2.3 Nucleation and growth

This section describes the growth of existing grains within the simulation. Nucleation of new crystal grains takes place within the molten region immediately beneath the laser spot. Note that, by virtue of the link between eqs. (2.6) and (2.9), grain growth of nucleated grains, i.e., interfacial motion, is anisotropic due to gradients in the temperature field.

Nucleation is modeled as a Poisson process controlled by the temperature at each respective mesh point. The critical radius and free energy for homogeneous nucleation is obtained via classical nucleation theory [80]:

$$\begin{aligned} R^*(T) &= \frac{2\gamma_i}{\Delta G(T)} = \frac{2\gamma_i}{\rho h_l \frac{T_m - T}{T_m}} = \frac{2\gamma_i T_m}{\rho h_l \Delta T} \\ \Delta G^*_{\text{hom}}(T) &= \frac{16\pi\gamma_i^3 T_m^2}{3\rho^2 h_l^2 \Delta T^2} \end{aligned} \tag{2.12}$$

where $\Delta T = T_m - T$ describes the undercooling. ΔT affects both the size of the critical radius and the free energy barrier for creating such a nucleus. As the undercooling increases –i.e., if the local temperature decreases–, both the critical radius and free energy barrier decrease.

In real materials, the nucleation rate is a temperature dependent feature, and homogeneous nucleation is effectively impractical on laboratory timescales. Considering that nucle-

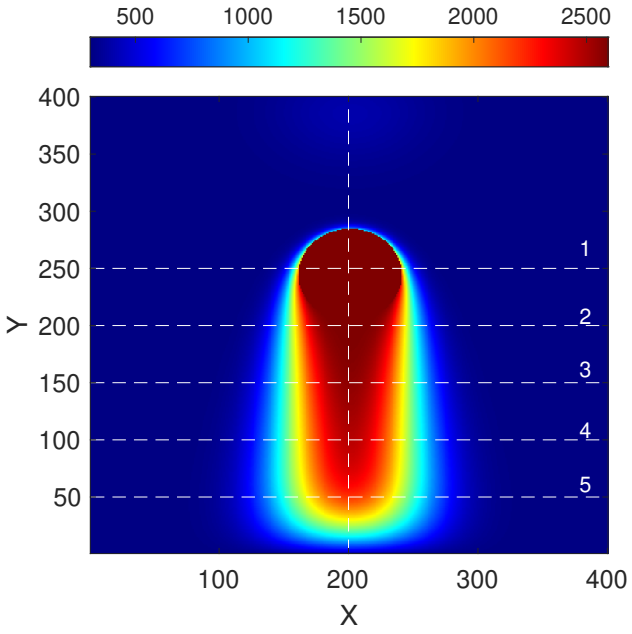

(a) 2D heat diffusion color map from moving laser spot.

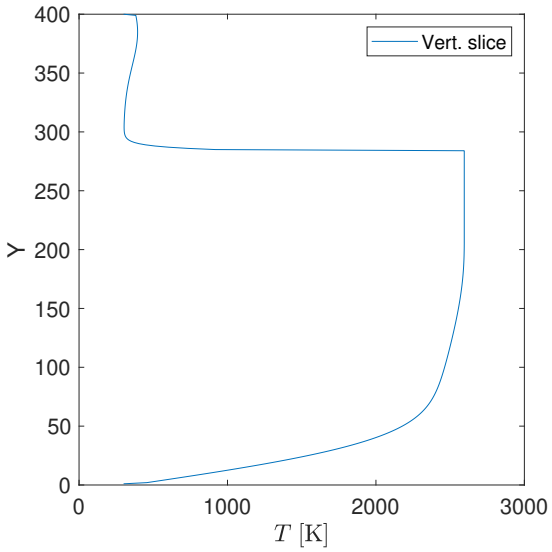

(b) Temperature profile from vertical slice at $x = 200\Delta x$.

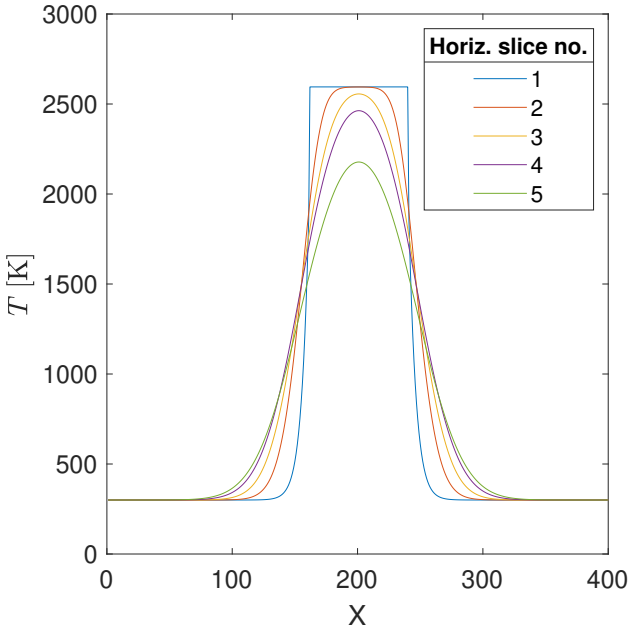

(c) Temperature profiles of horizontal slices in wake of laser spot.

Figure 2.4: Results from test case of implicit heat diffusion solver.

ation in AM processes is expected to occur on an existing substrate, we expect heterogeneous nucleation in all cases, which reduces the free energy barrier. The reduction in free energy

depends on the contact angle θ_c that the nucleus makes with the substrate.

$$\Delta G^*_{\text{het}}(T) = \Delta G^*_{\text{hom}}(T) \cdot f(\theta_c) \tag{2.13}$$

$$f(\theta_c) = \frac{2 - 3\cos\theta_c + \cos^3\theta_c}{4} \tag{2.14}$$

Defined in this way, $f(\theta_c)$ is a positive function between 0 and 1 (at 0° and 180°, respectively) with zero derivative at both ends [81]. Within classical nucleation theory, the nucleation rate per unit volume follows a thermally-activated expression [82, 83]:

$$J_{\text{het}}(T) = \frac{k_B T N_a}{h} \exp\left(-\frac{Q_d}{k_B T}\right) \exp\left(-\frac{\Delta G^*_{\text{het}}(T)}{k_B T}\right) \tag{2.15}$$

Here, N_a is the atomic density, h is Planck's constant, and Q_d is an activation energy. The effect of the contact angle θ_c on the nucleation rate is shown qualitatively in Figure 2.5, as the curves have been normalized against their respective maxima for better visibility. Of particular note is the shifting of the peak position due to the contact angle. As the contact angle approaches 180°, the peak moves toward the expected position for homogeneous nucleation, since $f(180°) = 1$.

The nucleation rate dictates the likelihood of a nucleation event, i.e., the insertion at a spatial point belonging to the untransformed region (i.e., with $\phi = 0$) of a solid nucleus with a critical size given by eq. (2.12). Since this is a probabilistic process, the nucleation probability has to be sampled appropriately at the beginning of each iteration for the volume of untransformed (superheated liquid) material in the simulation zone where Δt_{nuc} is the cumulative time since the last nucleation event took place. The pseudocode representing this direct nucleation criterion is described in Algorithm 1.

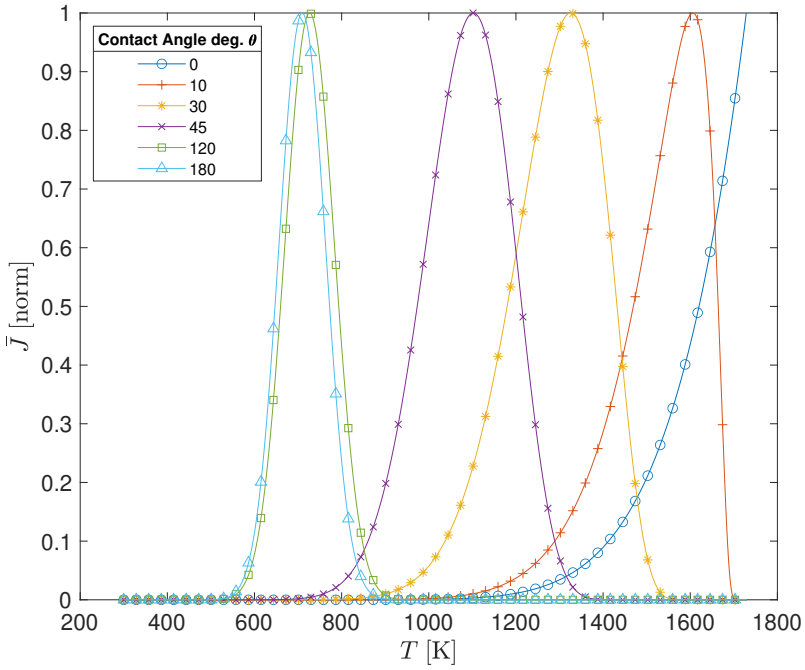

Figure 2.5: Normalized plots of heterogeneous nucleation rates as a function of temperature and nucleus contact angle with substrate, θ_c.

Algorithm 1 : Algorithm describing direct nucleation.

$P_{\text{nuc}} = J_{\text{het}} \cdot V_l \cdot \Delta t_{\text{nuc}}$
if $(P_{\text{nuc}} \geq 1)$ **then**
    Insert nucleus of size R^* at random point inside V_l.
else if $(P_{\text{nuc}} < 1)$ **then**
    Get: $\xi \in (0, 1]$
    if $(P_{\text{nuc}} > \xi)$ **then**
        Insert nucleus of size R^* at random point inside V_l.
        $V_l = V_l - \frac{4\pi}{3} (R^*)^3$
        $\Delta t_{\text{nuc}} = 0$
    else
        $\Delta t_{\text{nuc}} = \Delta t_{\text{nuc}} + \Delta t$
    end if
end if

For the procedure in Algorithm 1 to be strictly correct, the mesh size must satisfy $\Delta x \leq R^*$. Using the parameters given in Table 2.2, this implies considering values of less than 5.0 nm for Δx. Considering that the laser spot size is ≈ 0.4 mm in diameter, it would require more than 10^{10} mesh points to resolve the entire area of the melt pool under the laser, which is currently beyond our computational means for this work. Consequently, we modify the above procedure with one where nuclei are inserted with a size equal to that of the mesh, i.e., Δx. However, instead of advancing time by the prescribed timestep Δt, we advance the simulation clock by an amount commensurate with the length of time needed by the nucleus to grow from R^* to Δx. For this approach to be valid, the growth of critical nuclei from R^* to Δx must be much faster than any other process in the system. We believe this adiabatic approximation to be justified by (i) the large temperature difference between the areas near the melt pool and those far away from it, and (ii) by the much larger curvature of small growing nuclei relative to existing interfaces. Accordingly, time is advanced by an amount:

$$\Delta t_{\text{ad}} = \frac{\Delta x - R^*(T)}{v_{\text{int}}} = \frac{\Delta x - R^*(T)}{\Delta G_V(T) M(T)} = \frac{(\Delta x - R^*(T))\, T_m}{\rho h_l \Delta T M(T)} \tag{2.16}$$

where we have defined the velocity of the nuclei interface, v_{int}, as the product of the interface mobility times the free energy gain associated with nuclei rapid growth.

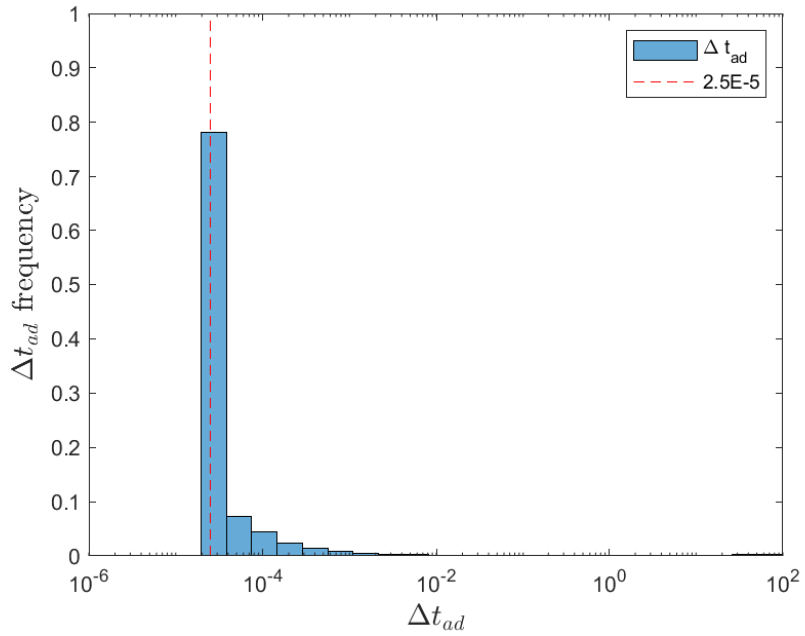

Figure 2.6: Histogram showing time step used per iteration. Δt_{ad} selected when $\Delta t_{ad} > \Delta t$.

2.2.4 Initial 2D Voronoi construction

The initial underlying substrate upon which the AM method runs is generated using a Voronoi tessellation of a $N \times M$ discrete square grid populated with K grain centers adhering to a log-normal distance distribution. Once all K grain centers are set, each mesh point p_i is assigned to the nearest center k_j after accounting for periodic boundary conditions where p_i^g denotes the grain assignment.

$$\begin{aligned} p_i^g &= \min\left[\text{dist}(p_i, k_j') : j \in \{1, ..., K\}\right] \\ \text{dist}(p_i, k_j') &= \sqrt{\left(p_{ix} - k_{jx}'\right)^2 + \left(p_{iy} - k_{jy}'\right)^2} \end{aligned} \tag{2.17}$$

Here k_j' denotes any of the points in the set of periodic Voronoi centers pertaining to center k_j. An example is shown schematically in Figure 2.7, where mesh point p is assigned to grain center k_1 despite being closer to grain center k_2 in the central simulation space. This is because the distance to the periodic virtual center k_1' is the shortest distance of those shown.

After assigning every mesh point to the corresponding grains, we build an orientation map for the entire structure generated by the so-called *de-centered octahedron algorithm* [84–86]. This approach is known to favor the formation of commonly observed $\langle 100 \rangle$ growth textures in cubic crystals [87–89]. The orientation map is expressed as Euler angles $[\phi_1, \Phi, \phi_2]$ and a grain identification number for later reference in the algorithm.

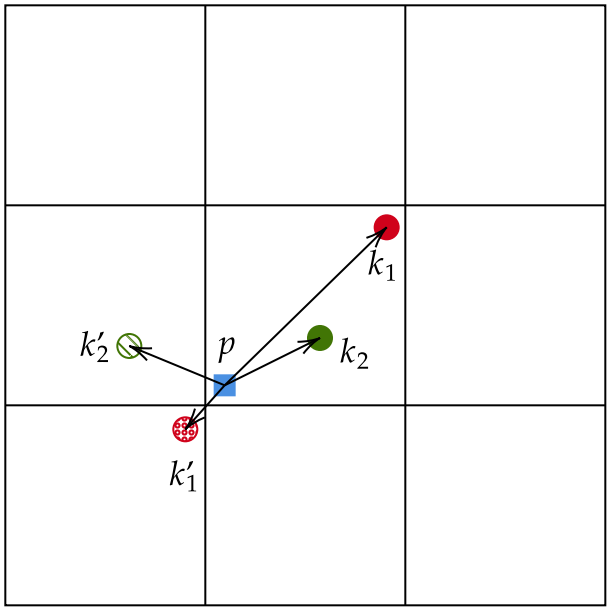

Figure 2.7: Schematic representation of periodic distance-checking for Voronoi diagram.

A verification example of a microstructure generated using the procedure just described is shown in Figures 2.8a and 2.8b.

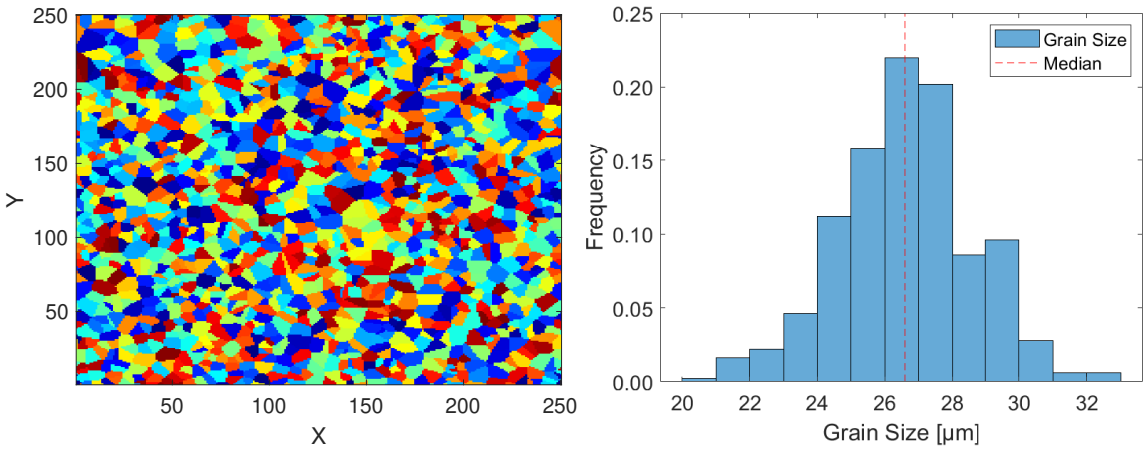

(a) (b)

Figure 2.8: (a) Example of initial substrate generated for use with first AM iteration. (b) Grain size distribution for substrate example shown.

2.3 Results

All simulations were run on a square mesh with 250 elements per side representing a total simulated area of 1.56 mm^2. The size of each mesh element and the time step used per iteration is shown in Table 2.2. The initial Voronoi substrate was created with 1500 centers to create a distribution with a median grain size of approximately 26.5 microns, which is consistent with values seen in empirical studies of AM 316L [66, 90]. The size of the mesh was chosen to balance performance with overall testing area, as the time per iteration scales quadratically with the mesh size, as shown in Fig. 2.9, where the time reported is averaged from 500 iterations of the code. Error bars are not shown on the plot as the standard error of each respective mean was less than 0.4% of the reported value. All simulations were run on a 3.61GHz Intel i7-12700K processor.

Figure 2.10 shows a series of snapshots detailing the microstructural evolution of the active layer in the wake of the laser spot for a case with $v_{\text{spot}} = 300$ mm·s^{-1}, $d_{\text{spot}} = 0.3$ mm, and $W_{\text{hatch}} = 1.7r_{\text{spot}} = 0.255$ mm. In Figs. 2.10a, 2.10d, and 2.10g, areas unassigned to any

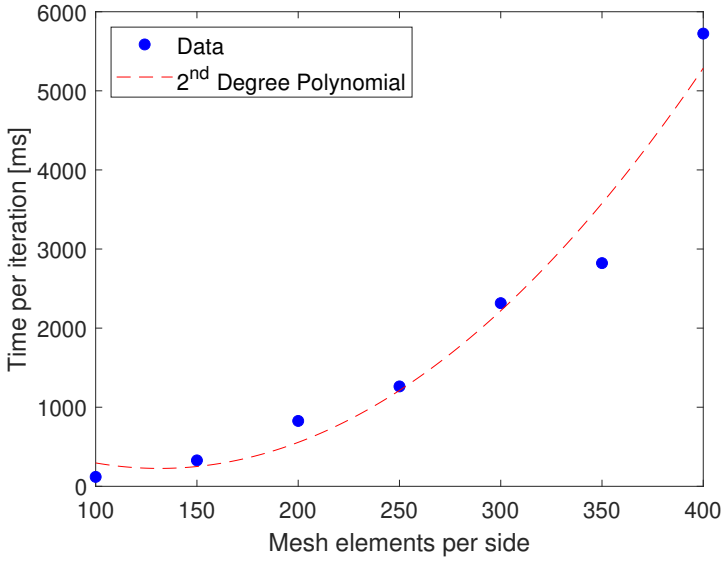

Figure 2.9: Time per iteration of code for increasing number of mesh elements in simulation. Time per iteration taken as average time of 500 iterations for each size shown.

new grains are shown in black, and the colored areas show individual grains (i.e., domains with the same crystal orientation). Figs. 2.10b, 2.10e, and 2.10h show the corresponding temperature fields. Nucleation is seen to occur in the wake of the beam as well on the edges of the boundaries of the heat envelope. These nuclei then grow anisotropically in response to the temperature gradient from the laser spot (as seen in empirical studies [91–93]). Figs. 2.10c, 2.10f, and 2.10i indicate the extent of the transformed microstructure. After the laser has fully swept the simulation area, this microstructure is used as the substrate for the next layer. Each run consisted of 50 laser spot passes to build up a 3D structure analogous to a columnar material. An example of a finalized microstructure is shown in Figure 2.11, with Fig. 2.11a showing a 3D perspective of the built microstructure, and 2.11b a cross-sectional cut along the plane indicated by a dashed white line in 2.11a. The simulated microstructures display a characteristic columnar structure, with a clear continuity in crystal orientation across the entire height (build direction) of the system. Similar structures are commonly seen during directional solidification, and, in the case of layer-by-layer growth, the columnar grains are seen to grow epitaxially from the previously deposited layer, along the build direction which

is perpendicular to the bottom of the melt pool [94–97]. In general, the columnar grains grow as the bottom the melt pool moves upwards during the subsequent cooling process. Thus, our model can be regarded as replicating a LPBF process with fast-cooling in the growth direction.

We then carried out 27 independent simulations with different permutations of the values in Table 2.1. The grain size of each layer was calculated using the linear intercept method with 50 vertical lines and 50 horizontal lines spaced equally in the mesh. The mean and standard error of each simulation plotted against the layer number is shown in Figure 2.12. In the figure, each row pertains to a single value for d_{spot} and each column pertains to a single v_{spot} value. In all simulations there is a trend showing the average grain size increases over the course of 50 laser passes, with the average final grain size calculated as 63.4 ± 7.4 μm. The largest grains across all simulations appear in the simulations with the shortest hatch width of $1.5r_{\text{spot}}$, while hatch widths $1.6r_{\text{spot}}$ and $1.7r_{\text{spot}}$ are within error of each other for almost all simulations. Increases in spot velocity tend to suppress grain growth for a given spot diameter, whereas increasing the spot diameter for a given fixed velocity tends to increase the maximum final average grain size.

The columnar grain area percentage was also calculated for every simulation per layer. Referencing the schematic provided in Figure 2.2, this metric was calculated by surveying each mesh point and counting any point in the active layer, N, that had the same grain orientation as the corresponding point in the underlying layer, $(N-1)$. This count was then divided by the number of total mesh points in the simulation to return an area percentage of the columnar grains. The results are shown in Figure 2.13, where a clear tendency can be observed for all simulations to increase in columnar grain area fraction, approaching an average maximum of 0.84 ± 0.01 area fraction. None of the input variables appear to be strongly correlated to the formation of columnar grains, as the values of all simulations are roughly similar.

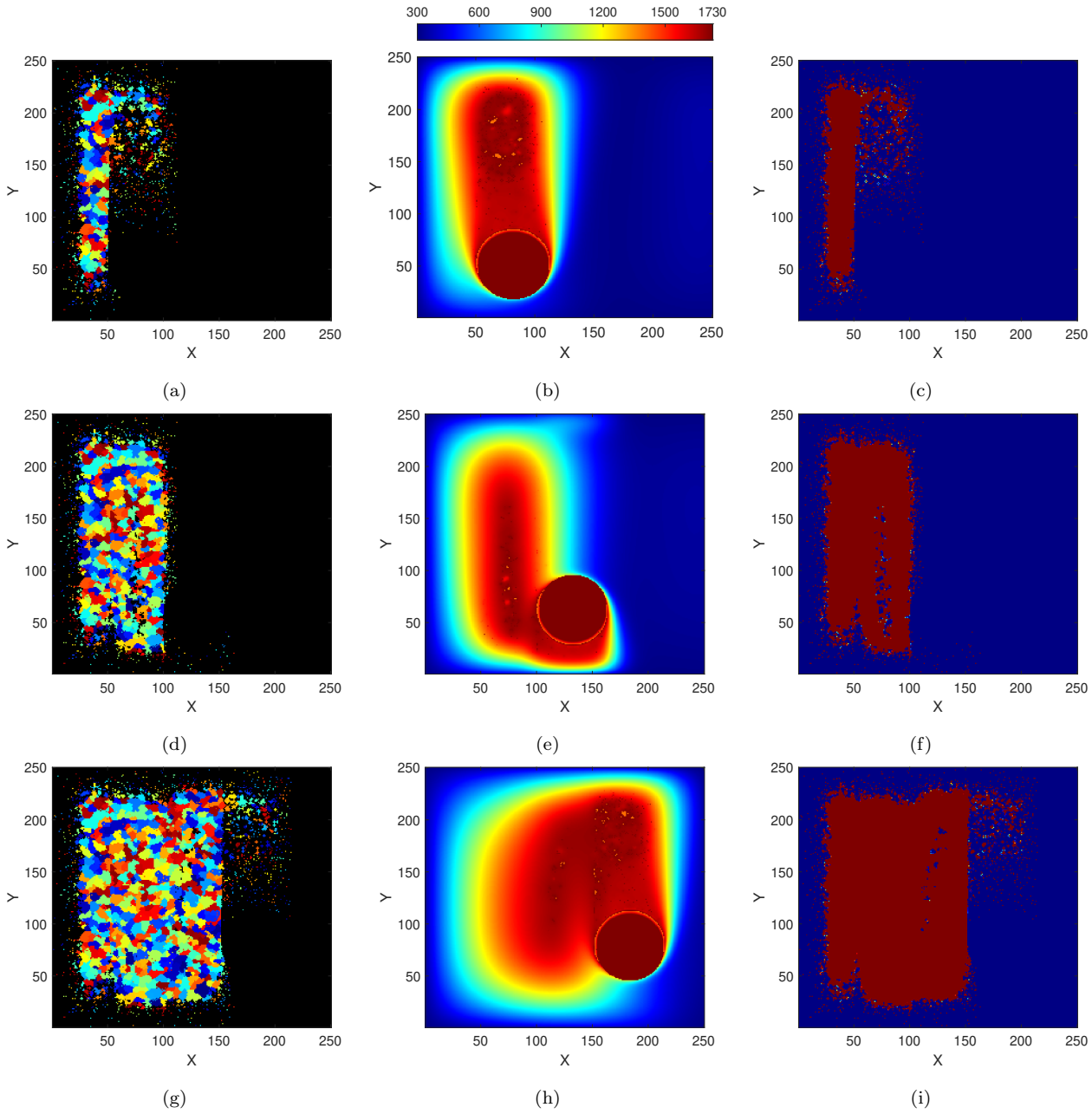

Figure 2.10: Sequence of simulation snapshots for a case with $v_{\text{spot}} = 300$ mm·s^{-1}, $d_{\text{spot}} = 0.3$ mm, and $W_{\text{hatch}} = 0.255$ mm. (a), (d), and (g) show the newly created grains and their orientations over the existing substrate. (b), (e), and (h) show the instantaneous temperature field, and (c), (f), and (i) show the area fraction of the transformed material. Solid nuclei can be appreciated in the molten region in the wake of the laser spot in (b), (e), and (h).

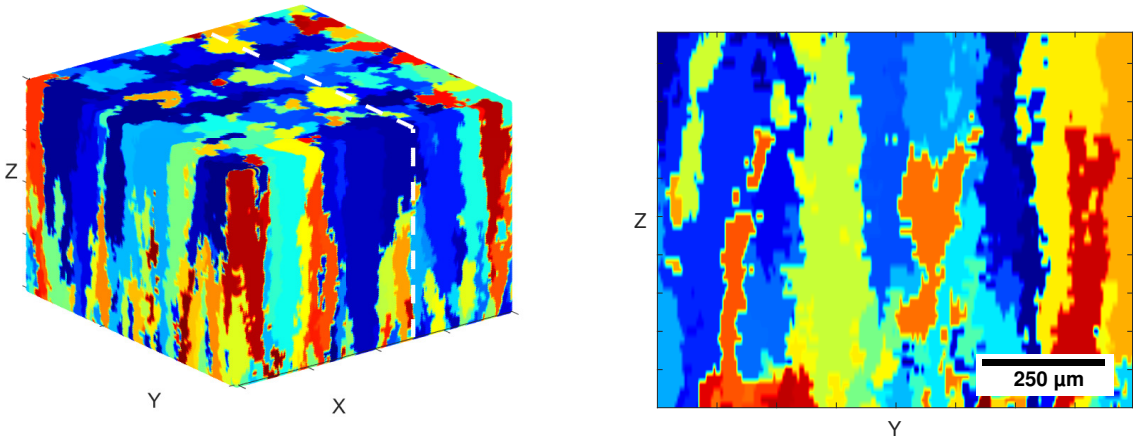

(a) (b)

Figure 2.11: Subsection of simulation output to highlight (a) 3D microstructure of final material with (b) vertical slice as shown by black lines.

2.4 Discussion

2.4.1 Simulation results

The present approach is a full thermo-physical phase field model that simulates the growth of metallic microstructures through additive layer buildup by laser melting. Our model captures melting, solidification by nucleation in the melt pool, solidification by growth of existing grains adjacent to the meltpool, and a full treatment of the temperature field by solving the heat equation coupled to phase field changes. The model is developed in two dimensions and neglects the granular structure of the powder layer. Instead, we assume that the unprocessed layer can be described by a uniform medium with a prescribed thickness. Strictly speaking, the 2D approach is valid when the thickness of the powder layer, Δh, is smaller than the characteristic heat diffusion mean free path, λ_h. In our case:

$$\lambda_h = \sqrt{\alpha_L \Delta t}$$

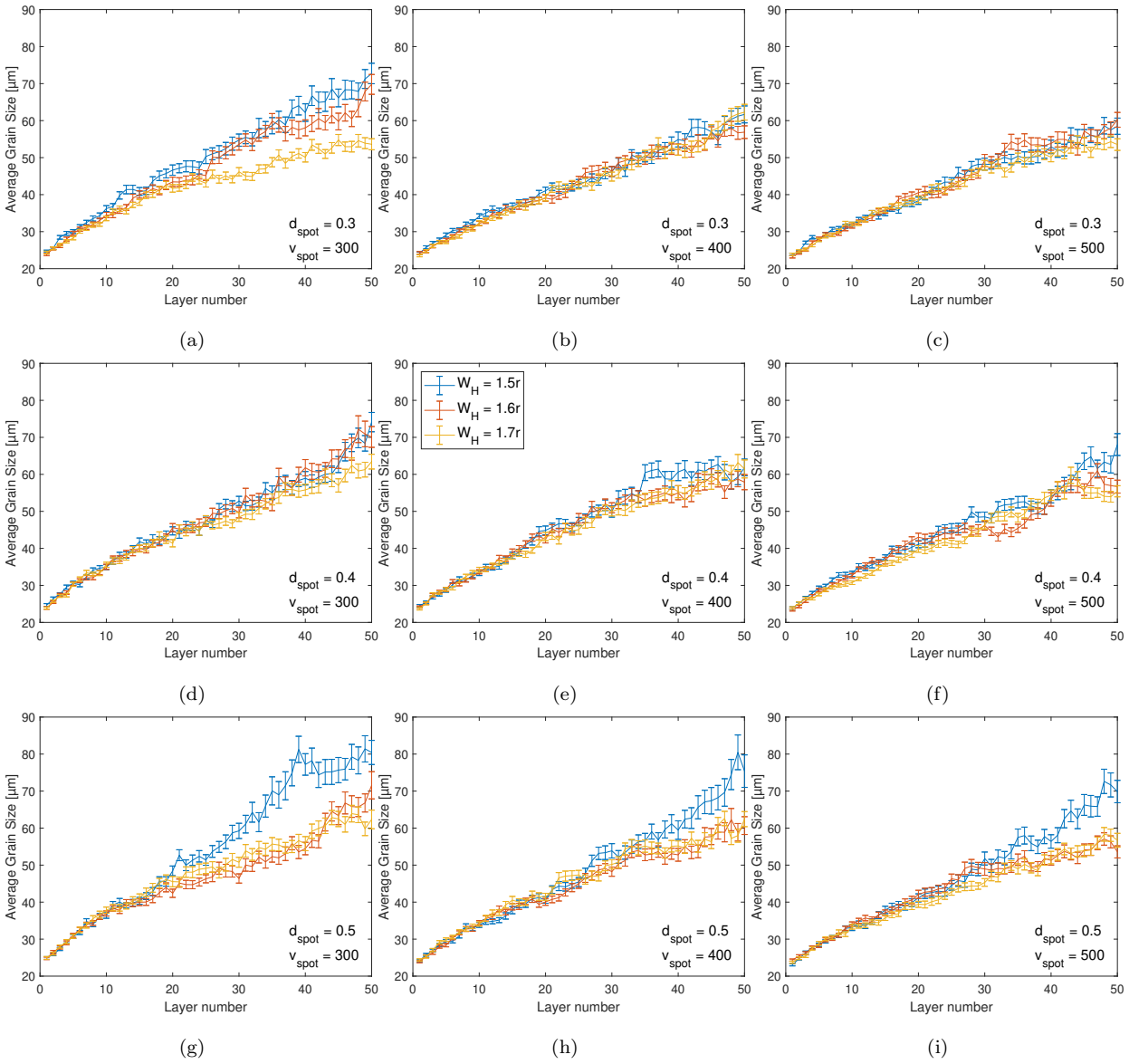

Figure 2.12: Average grain size evolution for all permutations of simulations run. All y-axes are set to the same scale for comparison.

Through eq. (2.8), Δt is connected to other simulations parameters:

$$\lambda_h < \sqrt{\frac{\alpha_L(\Delta x)^2}{4M_\phi a^2}}$$

which, for the values given in Table 2.2, gives a value of approximately $\Delta h < 16$ microns. Feedstock powders used as a raw material in LPBF have typical particle sizes ranging between

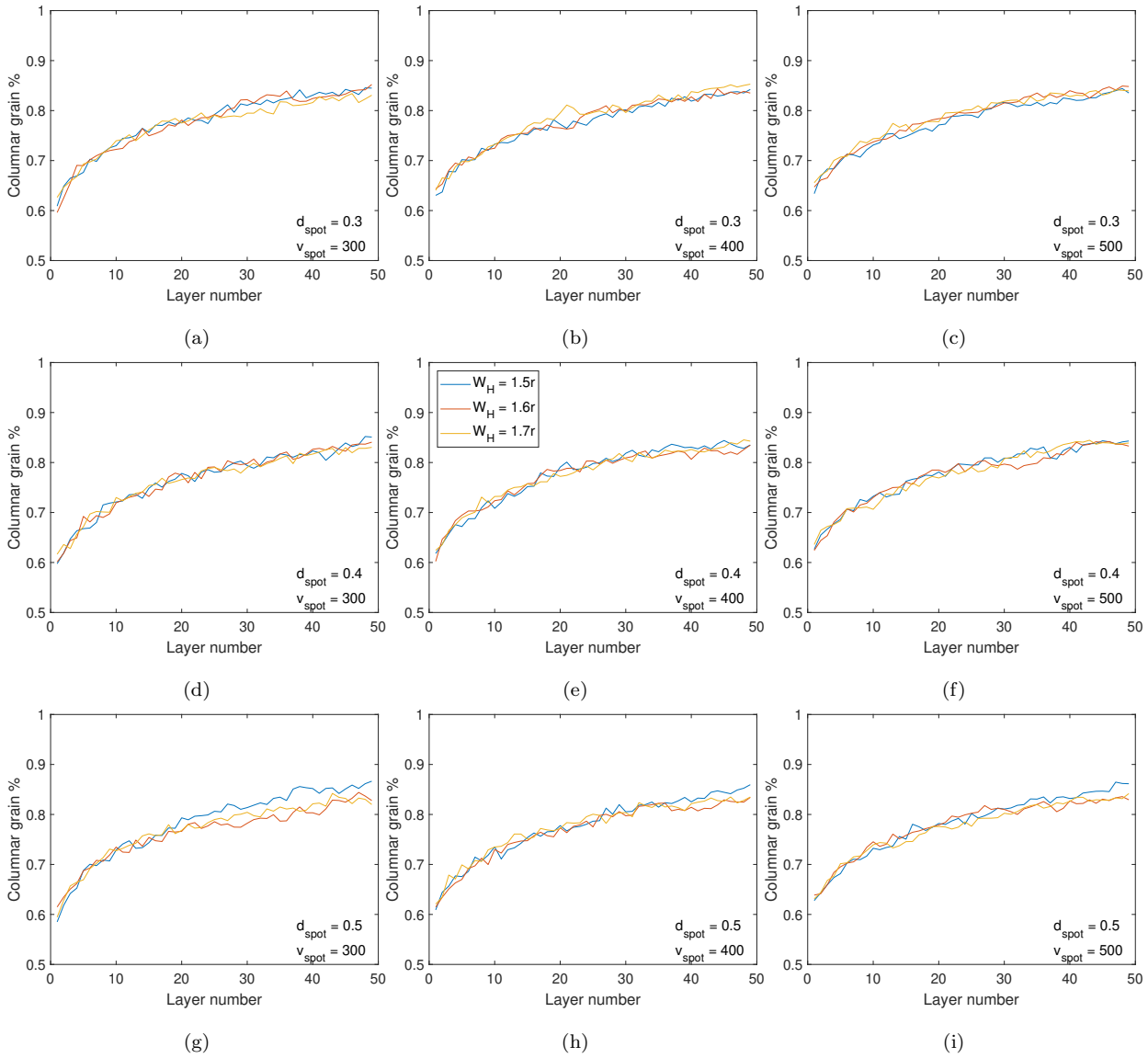

Figure 2.13: Interlayer mismatch percentage for all permutations of simulations run. All the vertical axes are set to the same scale for comparison.

10 and 60 microns [98–100], which then makes our study a valid approximation for powders with fine particle sizes. Our model can capture processing parameters such as the laser spot diameter, laser scan speed, and laser spot overlap in subsequent passes ('cross-hatching'). As such, we can assess the variables that have the most influence on final microstructure formation.

In particular, the results of the simulations show the effect of the input parameters on the outputs of grain size and area fraction pertaining to columnar grains. The simulations in this study only cover a limited section of the available parameter space with respect to both laser parameters and material properties. From the studies here, three main trends appear to emerge: (i) decreasing hatch width is positively correlated with increasing grain growth, (ii) increasing laser spot size is positively correlated with increased grain growth, 3) increasing laser raster velocity is negatively correlated with increased grain growth. Addressing the first point, hatch width would reasonably have a positive correlation on grain growth under the assumption that the active layer has not fully cooled before the next laser pass occurs. Under the assumption of full cooling, any hatch width would remelt the area under the laser spot, leaving the surrounding material mostly unaffected. However, in the case of the heat not fully diffusing before the next laser pass, a smaller hatch width could result in more residual heat in the simulation, allowing grain growth for a greater percentage of the simulation iterations. As was described in Section 2.1.1, the *cool-down* period was imposed to allow the material to cool to a temperature that inhibited grain growth before the next laser pass. However, the length of this *cool-down* was not set to be sufficiently long to allow all residual heat to dissipate, creating a central area of high temperature in the material. The cases of laser spot size and velocity have more apparent connections to enabling and inhibiting faster grain growth, respectively. Increasing the spot size melts more material in an iteration, and deposits more heat into the material since the temperature under the laser spot is fixed is a superheated state. On the contrary, increasing the spot velocity results is less residual heat within the material as the spot travels more during the simulated time step, resulting in fewer total iterations where the spot is active within the simulation space. Probably, there is a critical velocity for which the heat dissipation rate is comparable to the laser speed. Below this velocity heat dissipiation occurs on the same timescale as laser motion, favoring microstructures with equiaxed grains. Above this critical velocity, the grains are elongated in the processing plane.

In terms of the final microstructures obtained (e.g., Fig. 2.11), the columnar morphology is commonly observed during solidification, in the direction perpendicular to the melt pool's interface. With thin active layers, or under high laser power conditions, this growth can be observed directly along the build direction. Figure 2.14 provides a qualitative comparison between the simulated structures and experimental observations. For example, large columnar grains with high aspect ratio are seen to form in 316L stainless steel as a result of epitaxial growth when using a high laser power [101], see Figure 2.14b. Another example is shown in Figure 2.14c [102] in LBPF-fabricated Al-2.5Fe sample with $\dot{P} = 204$ W and $v = 600$ mm·s^{-1} (recall that our values are $\dot{P} = 230$ W and $v = 500$ mm·s^{-1}, Tables 2.1 and 2.2). Notwithstanding the uncertainties in some of the computational parameters and the modeling assumptions, the level of qualitative agreement in the comparison between our simulated microstructures and those experimentally observed under similar conditions is encouraging.

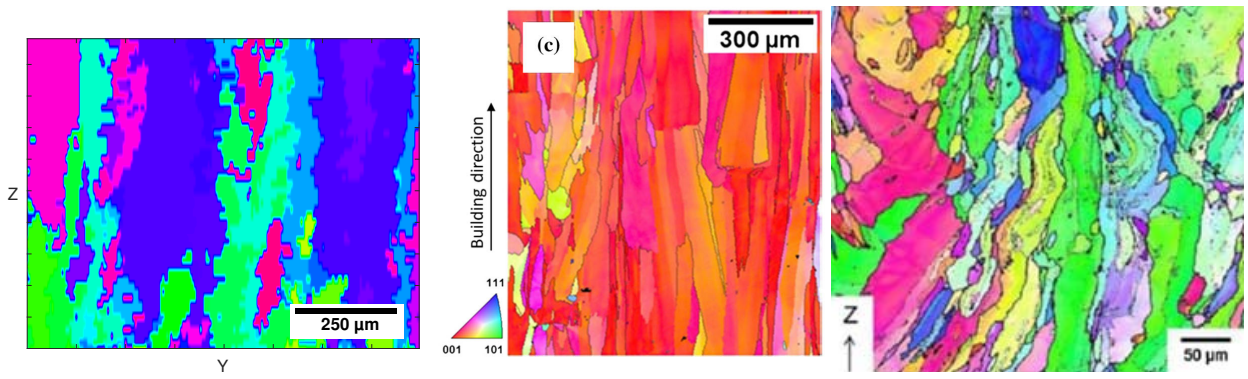

(a) This work (b) LPBF 316L steel [101] (c) LPBF Al-2.5Fe [102]

Figure 2.14: Qualitative comparison between simulated and experimental microstructures. (a) Exemplar of a microstructure generated in this work. (b) Columnar structure in 316L stainless steel as a result of epitaxial growth under high laser power [101]. (c) Fabricated Al-2.5Fe sample with $\dot{P} = 204$ W and $v = 600$ mm·s^{-1} [102]. The growth direction is the same in all cases (vertical direction of the paper). All the colors refer to the stereographic triangle shown.

On the topic of parameter variability, investigating the effect of materials properties on simulation outcomes needs to be a priority of future studies. For example, the effect of the mobility prefactor M_0 on microstructure and columnar grain area fraction is an aspect worth

studying. Increasing this parameter would make the simulation more growth-dominated, as the phase field solver would grow into warmer mesh points more readily than the present study, creating grains with more elongated features. Given the variability reported in the literature on the value of this prefactor, future studies may compare how well different values of M_0 compare to empirical studies of a given material.

2.4.2 Model limitations

It is valuable to discuss the limitations of the model and avenues for improvement in future iterations. To begin, the simulated area of the model is on the order of 1 mm^2, which is suitable for incipient studies of bulk microstructure, but requires a coarse mesh size to be computationally viable. This inherently introduces inaccuracies as the minimum resolution of the mesh may prohibit the appearance of some microstructural features. Continuing to consider the time-cost of computation, the code developed for this model was not designed for parallel computing, but would likely benefit from parallel computing since the calculations for the phase field and temperature field could be calculated concurrently.

Continuing with the 2D nature of the present model, it is currently not designed to resolve the shape of a melt pool in three dimensions, the diffusion of heat through the previously fused metallic layers, or heat diffusion into the atmosphere and the leftover powder surrounding the fused material.

The model also makes assumptions regarding the behavior of the deposited powder in the actively melting layer, including (i) the code ignores the granular structure of the powders, (ii) the powders completely melt into the liquid phase, (iii) there is no incomplete fusion in the completed layer, all mesh points are assigned a grain ID and orientation. The model therefore does not account for the defects that can appear in a fused layer as a result of porosity [103, 104], hot cracking [105, 106], balling [107, 108], and lack-of-fusion [109–111]. Including these types of defects in future iterations of the model would output microstructures that more accurately represent what is seen in empirical bulk studies. This would also make the

model suitable for use in studies of mechanical properties, as these defects would introduce deleterious effects to a components' mechanical behavior.

In terms of the heat diffusion solver implemented in the model, the only limitation worth mentioning is that associated with the heterogeneous nucleation provided in the model. The model assumes all points are subjected to the same nucleation conditions, whereas true materials would have preferential nucleation sites such as solid grains that did not completely melt, or areas on the boundary of the melt pool. The melt pool edge behavior is captured to some degree by the higher probability of nucleation based on temperature as shown in Figure 2.5, but this behavior is not mathematically modeled in the current program. The nucleation in this model also does not account for the boundary energy introduced through preferential cubic crystal orientations like $\langle 100 \rangle$, $\langle 110 \rangle$, or $\langle 111 \rangle$.

2.5 Conclusions

We finalize the paper with our most important conclusions :

1. We have developed a thermally informed phase field model capable of simulating the heterogeneous nucleation and growth of additively-manufactured metallic materials to study the presence of columnar grain growth in the build direction.

2. An explicit Euler discretization of the phase field in combination with an implicit Euler discretization of the heat diffusion equation aligns the iterative solutions in both space and time, which allows for accurate modeling of the melting and re-solidification of metal material in the path of a moving laser spot with variable parameters.

3. The model assumes that the layer-by-layer buildup of material follows a crystallographic continuity along the build direction, enabled by heterogeneous nucleation and growth of new grains on existing grains in the underlying substrate layer. We find that the average grain size gradually increases with the build direction (giving a microstruc-

ture with ‘top-heavy’ columnar grains).

4. We have presented correlations between the input parameters of spot size, scan velocity, and hatch width on the grain growth seen in successive layers of the simulated material.

CHAPTER 3

Finite element crystal plasticity simulations

3.1 Numerical model

3.1.1 Diffuse Crystal Interface Plasticity Model

The following is a brief description of the previously-developed diffuse crystal interface plasticity model employed here. The original work can be found in ref.[61]. The basis of the diffuse-crystal interface model is to identify dislocations as the basic carrier of plastic deformation and build grain boundaries as continuum aggregates of these defects. In this fashion, grain boundaries are seen as incompatibilities of a plastic rotation field, which –much in the manner of standard elasto-plastic decompositions– must be closed by defining a special class of geometrically-necessary dislocations (GND) that habit the GB plane. Crystal deformation is modeled in the traditional sense, as a multiplicative combination of elastic and plastic deformations:

$$\boldsymbol{F}\left(\boldsymbol{X},t\right)=\boldsymbol{F}^{L}\left(\boldsymbol{X},t\right)\boldsymbol{F}^{P}\left(\boldsymbol{X},t\right) \tag{3.1}$$

where $\boldsymbol{F}^{L}$ and $\boldsymbol{F}^{P}$ are the lattice and plastic components of the total deformation gradient $\boldsymbol{F}$, respectively, at time t and position $\boldsymbol{X}$. The evolution of $\boldsymbol{F}^{P}$ is determined through the contribution of slip systems via slip rates using the flow rule:

$$\dot{\boldsymbol{F}}^{P}=\boldsymbol{L}^{P}\boldsymbol{F}^{P} \tag{3.2}$$

Previously published in *Computational Materials Science*

$\boldsymbol{L}^P$ is the plastic velocity gradient, defined as:

$$\boldsymbol{L}^P(\boldsymbol{X},t) := \sum_{\alpha=1^N} \gamma^\alpha \boldsymbol{s}^\alpha \otimes \boldsymbol{m}^\alpha \tag{3.3}$$

where $\boldsymbol{s}^\alpha$ and $\boldsymbol{n}^\alpha$ are unit vectors representing the glide and plane normal directions for slip system α. The value γ^α corresponds to the crystallographic slip rate on each slip system. The additional microscopic force and energy balance considerations are described in ref.[61]. Using standard crystal plasticity methods, a stress-free single crystal is constructed at $t = 0$ by requiring that:

$$\boldsymbol{F}^L(\boldsymbol{X},0) = \boldsymbol{F}^P(\boldsymbol{X},0) \equiv \boldsymbol{I} \tag{3.4}$$

such that $\boldsymbol{F} \equiv \boldsymbol{I}$. In contrast, the diffuse crystal interface model sets the initial state of the polycrystal to be:

$$\boldsymbol{F}^L(\boldsymbol{X},0) = \boldsymbol{R}^0(\boldsymbol{X}), \qquad \boldsymbol{F}^P(\boldsymbol{X},0) = \boldsymbol{R}^0(\boldsymbol{X})^T \tag{3.5}$$

where $\boldsymbol{R}^0$ represent the lattice rotation field in the polycrystal and maintains piecewise-constant values in each grain and smooth transitions across grain boundaries.

The rotational decomposition expressed in eq.(3.5) is the central framework to the diffuse-crystal interface plasticity model employed here. Using this decomposition, we can study polycrystals as a single boundary-value problem. Numerical discontinuities in $\boldsymbol{F}^L$ and $\boldsymbol{F}^P$ are avoided by implementing a smoothed step function in the space of the rotational fields. The remainder of the grain boundary and finite element numerical procedures remain the same as described in ref.[61]. However, the constitutive equations for plastic flow have been modified to accommodate the allotropic nature of α/β-Ti and the changes are described in Section 3.1.2.

3.1.2 Dislocation evolution model

The dual-phase nature of Ti-6Al-4V results in complex plastic deformation mechanisms that are not easily modeled. The microscopic force balance used here [61] is an extension of the

approach developed by Barton *et* al. in [112] for BCC crystals, not applicable to the HCP α phase. For α-Ti, we adopt the model by Moore *et* al.[113], which is also based on a Kocks-Mecking dislocation density evolution law:

$$\dot{\rho} = (k_1\sqrt{\rho} - k_2\rho)\sum_{\alpha}^{N} |\dot{\gamma}^{\alpha}| \tag{3.6}$$

where ρ is the dislocation density, k_1 is the hardening parameter, k_2 is the recovery parameter, and $\sum_{\alpha}^{N} |\dot{\gamma}^{\alpha}|$ is the total shear rate. Limited hardening has been seen in near-α alloys in the elasto-plastic transient range [113], and thus we set k_2 to zero. The evolving dislocation density is used to calculate the slip system strength through:

$$g^{\alpha} = w^{\alpha}\left(g_0 + \tilde{\alpha}Gb\sqrt{\rho}\right) \tag{3.7}$$

where g_0 is the lattice resistance, G is the shear modulus, b is the Burgers vector's modulus, and $\tilde{\alpha}$ is a material parameter that captures latent hardening. The anisotropy of the HCP crystal is embodied in the varying weights symbolized by the variable w^{α} which takes values of 1.0, 1.0, 1.1, and 3.0 for slip on the basal <a>, prismatic <a>, pyramidal <a>, and pyramidal <c+a>, respectively [114–116]. The inclusion of the slip system weight is one of the primary modifications to the plasticity model previously used in ref.[61] that enables extension to an allotropic HCP polycrystal. Lastly, the shear rates follow the standard strain-rate sensitivity dependence on stress, i.e.:

$$\dot{\gamma^{\alpha}} = \dot{\gamma}_0 \left|\frac{\tau^{\alpha}}{g^{\alpha}}\right|^{\frac{1}{m}} \mathrm{sign}(\tau^{\alpha}) \tag{3.8}$$

where $\dot{\gamma}_0$ is a reference slip rate, τ^{α} is the resolved shear stress, g^{α} is the crystal strength, and m is the strain rate sensitivity exponent. τ^{α} is obtained as the Schmid projection on slip system α of the Cauchy stress, $\boldsymbol{\sigma}$:

$$\tau^{\alpha} = \boldsymbol{s}^{\alpha} \cdot \boldsymbol{\sigma} \cdot \boldsymbol{m}^{\alpha} \tag{3.9}$$

with:

$$\boldsymbol{\sigma} := \frac{\mathcal{C}}{2}\left(\boldsymbol{F}^{T}\boldsymbol{F} - \boldsymbol{I}\right) \tag{3.10}$$

where $\mathcal{C}$ is the elasticity matrix. The system of equations provided in eqs. (3.1) to (3.10) is solved using a finite element approach in systems containing large numbers of grains, as described in 3.A. A description of the procedure used to construct the crystals is given in 3.B. The relevant modeling parameters used throughout the simulations are given in Table 3.1. The $\dot{\alpha}$, γ_o, m, and b parameters were adopted from ref. [113] and ρ_0 (initial dislocation density) was taken as 10^{12} m^{-2}, which is a reasonable value for the HCP [117] and BCC [61] phases. The k_1 and g_0 parameters were used to fit the model to literature data. The use of a single crystal strength parameter, g_o, was adopted for model simplicity. While the α and β slip systems certainly have different crystal strengths the priority of the exercise was to utilize the CPFE approach to generate adequate data to train a predictive regressor. The result of

Parameter	Value	Units
k_1	700	–
g_0	322.2	MPa
b	3×10^{-10}	m
ρ_0	10^{12}	m^{-2}
$\tilde{\alpha}$	0.5	–
m	0.02	–
γ_0	0.001	s^{-1}

Table 3.1: Simulation parameters used in the finite element simulations.

a simulated tensile test using a 90%/10% α/β equiaxed polycrystal is shown in Figure 3.1a along with a handful of tensile testing results of Ti-6Al-4V from the literature. The results of tensile loading a single crystal of α-Ti in the basal, prismatic, and pyramidal orientations is shown in Fig. 3.1b. The anisotropy of the HCP α phase is clearly demonstrated through the varying mechanical response to the different loading orientations. As expected, under basal loading conditions the crystal appears 'soft' while under prismatic loading conditions the crystal appears 'hard'. As well, the strength for two orientations of β-Ti are also shown,

a ‘soft’ one (loading along a direction near the middle of the standard triangle) and a ‘hard’ one (a vertex of the triangle). As the results show, the α phase can always produce a harder response compared to the BCC β one (partly due to an increased number of available slip systems in the HCP phase, see 3.A). The β phase has similarly been observed to deform more easily than the α phase in experimental studies [118–120].

A demonstration of the initial configuration of a dual phase crystal is provided in Figure 3.2 as a function of both phase and texture distribution. For clarity, the initial configuration shown in Fig. 3.2 is not the configuration that was used to find the data shown in Fig. 3.1a.

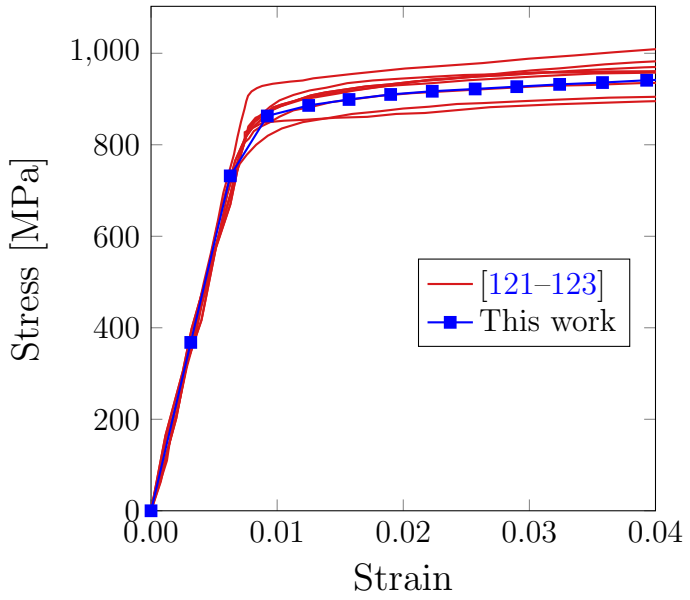

(a)

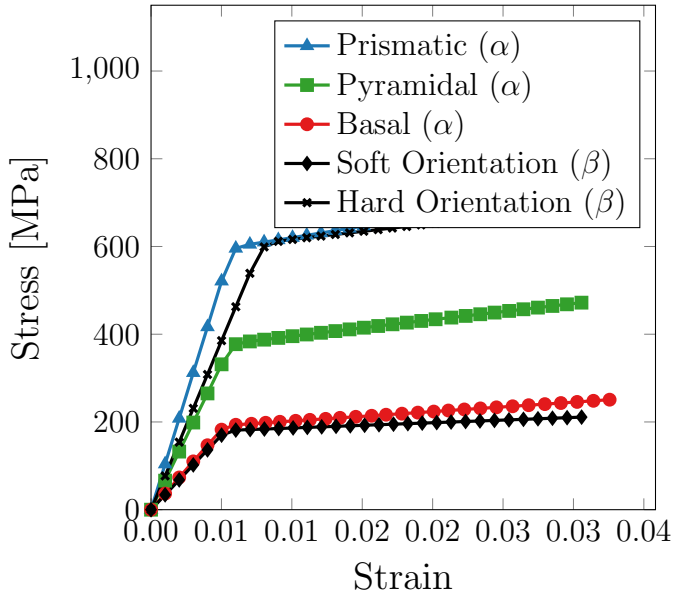

(b)

Figure 3.1: (a) Stress-strain curves of a simulated 90/10 α/β polycrystal along with a handful of literature results [121–123]. (b) Simulated tensile testing results from an α-Ti single crystal demonstrating the anisotropic mechanical response of the HCP lattice. Included is a β-Ti single crystal with a random orientation.

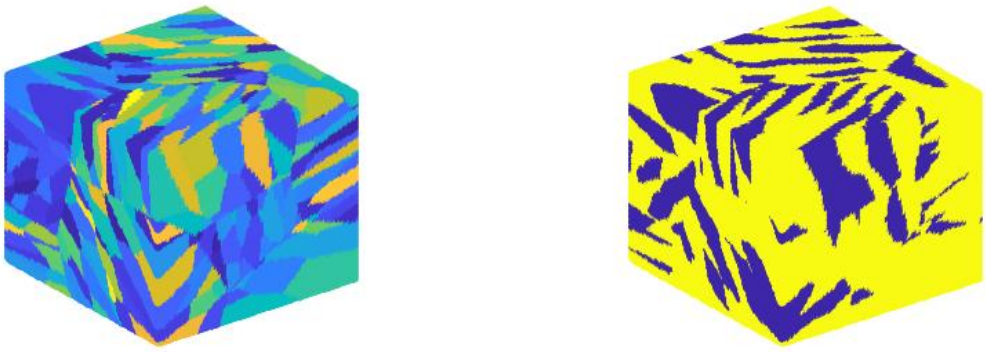

(a) (b)

Figure 3.2: A 90/10 α/β dual-phase microcrystal in which the coloring represents (a) uniquely oriented lamellae layers and (b) grain composition by color: α (blue) or β (yellow).

For this study we focus on the influence of grain geometry, grain size, strain rate, and α/β volume fraction as contributing factors to the microstructure-controlled strength. Grain geometry refers to the α/β "packets" within the microcrystal. The three grain geometries considered are equiaxed, platelet, and needle, exemplars of which are shown in Figure 3.3. Grain size refers to the "packet size" of α/β lamellae. This is an important distinction as each packet is composed of many individual lamellae layers that are approximately 0.5-3 μm thick. For further clarity please refer to the description of the crystal construction in 3.B. All microstructures were loaded in uniaxial tension along their principal length axis, which was made to coincide with the x direction, as shown in Figure 3.3.

3.2 Machine Learning Prediction of Strength and Hardening

Modern crystal plasticity finite element (CPFE) models are continuously improved with the addition of relevant mechanistic information and increased parameter accuracy. These mod-

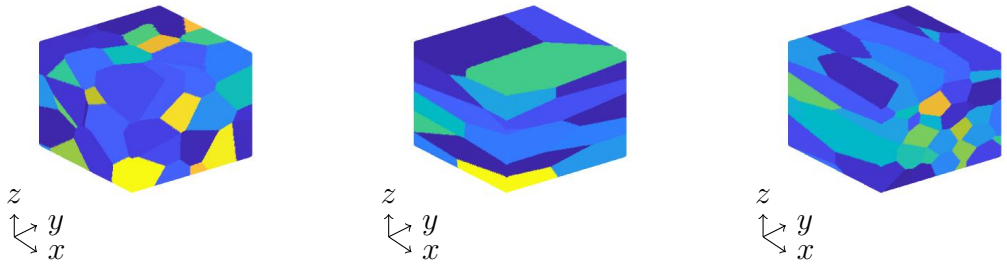

(a) (b) (c)

Figure 3.3: Examples of the (a) equiaxed, (b) plate, and (c) needle microstructures. Each color represents a single grain that would contain a packet of uniquely oriented α/β lamellae. All microstructures were placed under uniaxial tension in the x direction.

els complement and accelerate experimental efforts by providing indications of pathways to achieve a desired material performance. However, advanced CPFE models are often overly sensitive to certain input parameters and initial conditions and microstructures, making it difficult to parse through extended parameter sets and simulation conditions. In addition, the computational time required to simulate the necessary combinations of unique initial microstructures is not negligible. Therefore, developing a holistic understanding of a material's parametric features is often non-trivial. This effort can be aided by machine learning where regression techniques can be used to generalize the output of CPFE and predict desired micromechanical properties of crystals. Machine learning also provides insight into the importance of different microstructural features to better guide experimental efforts towards the most influential characteristics. In this study we use a supervised machine learning approach to develop several regression models that can assist in the prediction of the mechanical response of a dual-phase titanium polycrystal, namely, the yield strength and hardening rate. Table 3.2 provides a list of the models utilized in this study and their associated abbreviations. A brief mathematical description of each model is provided in 3.C. More thorough mathematical descriptions can be found in the references listed in Table 3.2. Both linear models (e.g., linear regression) and non-linear models (e.g. artificial neural net-

work) were chosen in order to approach the regression exercise with methods that range in complexity. In this way, the simple linear models act as a control condition. Moreover, it has been demonstrated that different regression techniques performer better/worse on different types of data [124–126]. Prior to running a large scale study it is difficult to assess which type of model will perform best, and therefore, we opted to include a variety of regression techniques.

Abbreviation	Model	References
LR	Linear Regression	[127]
R-LR	Ridge Linear Regression	[127]
KNN	K-Nearest Neighbors Regression	[127]
RT	Regression Tree	[127]
RF-R	Random Forest Regression	[128, 129]
XGB	`XgBoost`	[124, 130]
GB-R	Gradient Booster Regression	[131–133]
ANN	Artificial Neural Network	[134, 135]

Table 3.2: List of the models used and their associated abbreviations.

3.2.1 Evaluation Metrics

Next we define a series of relevant evaluation metrics common to all the regression models:

1. The mean-absolute error (MAE) is the mean of the absolute differences from the predicted y^i, and true $\hat{y}$ data from a sampling set of size n. The equation is given as:

$$\text{MAE} = \frac{1}{n}\sum_{i=1}^{n}\left|y^i - \hat{y}\right| \tag{3.11}$$

2. The root mean-squared error (RMSE) is the mean square difference from the predicted data and true data. The RMSE is more sensitive to outliers than the MAE and the

equation is given as:

$$\text{RMSE} = \sqrt{\frac{1}{n}\sum_{i=1}^{n}\left(y^i - \hat{y}\right)^2} \tag{3.12}$$

3. The R^2 score is a general fit of measure from a predicted regression curve to the original set of data on a scale from 0 (worst) to 1 (perfect). The equation for R^2 is:

$$R^2 = 1 - \frac{\sum_{i=1}^{n}\left(y^i - \hat{y}\right)^2}{\sum_{i=1}^{n}\left(y^i - \bar{y}\right)^2} \tag{3.13}$$

4. Lastly, the Pearson's correlation coefficient (PCC) is used during the results discussion and is described here. The PCC describes the linear correlation between two random variables on a normalized scale between 1 and -1. The measure of 1 being a perfect positive linear correlation and -1 being a perfect negative linear correlation. PCC does not capture non-linear relationships. The equation for PCC is:

$$\rho_{X,Y} = \frac{\text{cov}(X,Y)}{\sigma_X \sigma_Y} = \frac{\mathbb{E}[(X - \mu_X)(Y - \mu_Y)]}{\sigma_X \sigma_Y} \tag{3.14}$$

where $\mathbb{E}(x)$ is the expected value of x, μ_X and μ_Y are the means of X and Y, and σ_X and σ_Y their standard deviations. The expectation operator $\mathbb{E}$ here describes the arithmetic mean of the product of individual differences between the random variables (X, Y) and their respective means.

All models were implemented using the `scikit-learn` library and `xgboost` library in `Python` [130, 136]. 8-fold cross-validation was used during training.

3.3 Results

3.3.1 Plasticity Model Results

Crystals were constructed using a four-dimensional parameter vector whose components are given in Table 3.3. The matrix of combinations that results from exploring these four

dimensions amounts to 567 unique points in parameter space ($9 \times 7 \times 3 \times 3$ matrix), each of which was run four independent times to ensure numerical consistency and –when relevant– statistical validity. Thus, a total of 2268 finite element simulations were run over the course of this work. Data points were generated at random within the intervals specified in Table 3.3.

For each simulation, the yield strength was measured by the 0.2%-strain offset rule and the hardening rate was determined as the linear slope of stress-strain curve after yield.

Parameter	Values	Units
β fraction	5, 10, 15, 20, 25, 30, 35, 40, 45	vol.%
Grain Size	10, 12, 14, 17, 23, 25, 30	μm
Strain Rate	1.0, 5.0, 10.0	10^{-3} s^{-1}
Grain Geometry	Equiaxed, needle, platelet	–

Table 3.3: Input values for crystal formation used in finite element simulations.

Figure 3.4 shows the distribution of yield strength and hardening rate as a function of strain rate, β volume fraction, and grain geometry. All subplots contain the same data though different combinations of the input features are used to demonstrate trends in the crystal's mechanical response. In Figure 3.4a, the data show that β fraction and strain rate both positively correlate to yield strength, as shown by the tendency for larger red circles on exist the right side of the plot. It is also apparent that the highest hardening rates are typically observed with the lowest strain rate and highest β fraction samples. Figure 3.4b demonstrates that the grain size has a definite positive correlation with the hardening rate for certain samples. The relationship between grain size and yield strength is not discernible from the data shown. As well, grain geometry does not appear to have a clear correlation with either hardening rate or yield strength.

Figure 3.4c reinforces the observations that the lowest β fraction samples exhibit the

lowest yield strength and hardening rate while the highest β fraction samples exhibit the highest yield strength and hardening rate. This effect is amplified as the grains get smaller.

Figure 3.5 shows histograms of hardening rate and yield strength for the all data captured during parametric sweep (data shown in Figs. 3.4a to 3.4c. The mean value of each parameter is shown, as well as the value of the first three standard deviations. These markers can be used in coordination with the previous plots to determine the samples that fall more than three standard deviations from the mean and can therefore be considered outliers. The hardening rate data shows a measured mean value of 2.69 GPa with a standard deviation of 1.94 GPa. The yield strength data showed a measured mean value of 883.4 MPa with a standard deviation of 36.5 MPa. Using these criteria, 18 outliers were found, 13 based on hardening rate and 5 based on yield strength. Further examination of the outliers showed each had 4 or fewer grains of 25 μm or larger, 12 had 45% β fraction, 13 had an input strain rate of 10^{-3} s^{-1}.

Figure 3.6 shows the yield strength or hardening rate as a function of two input parameters. Each row of plots have the same input parameters for ease of comparison. Plots 3.6a and 3.6b show the yield strength and hardening rate versus strain rate and β fraction. Plots 3.6c and 3.6d show the same outputs as a function of grain size and β fraction. Plots 3.6e and 3.6f show the outputs versus grain geometry and grain size. Each plot shows all non-zero data from the simulated data set.

Synthesizing the information shown in Figures 3.6a and 3.6b, we see that increasing the β fraction and strain rate together results in increasing yield strengths, but does not contribute to increasing hardening rates. With respect to yield strength, increasing the strain rate from $\dot{\varepsilon} = 0.001$ s^{-1} to $\dot{\varepsilon} = 0.005$ s^{-1} has less effect than changing the strain rate the same amount up to $\dot{\varepsilon} = 0.01$ s^{-1}. In contrast, the largest increase in hardening rate is seen at high β percentage and low strain rate. By the information in these two plots, β percentage alone is not enough to control both the yield strength and post-yield hardening rate. A combination of β percentage and strain rate would be necessary to tune the output yield strength and

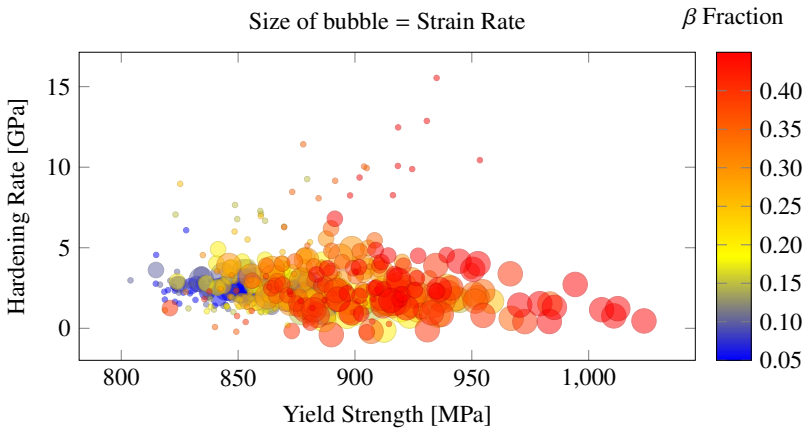

(a)

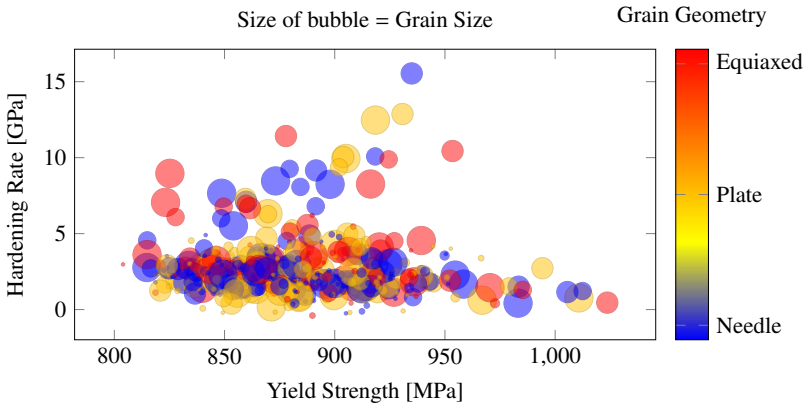

(b)

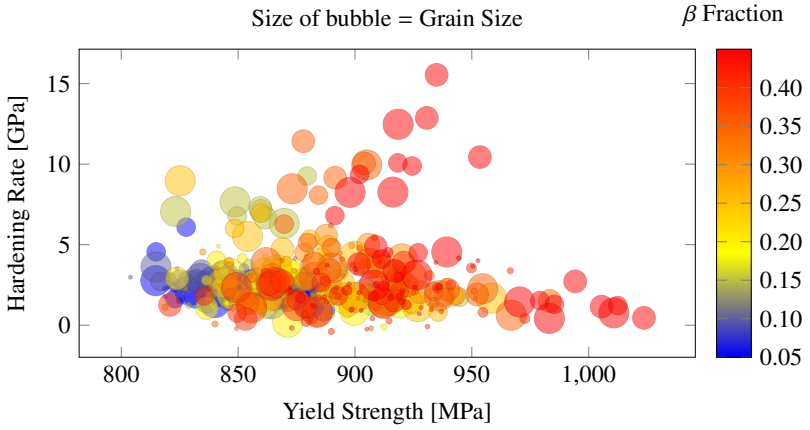

(c)

Figure 3.4: Hardening rate and yield strength distributions for all "gridded" simulations. Same data displayed for each plot with color/bubble size discrimination added for (a) strain rate and β fraction, (b) grain size and grain geometry, and (c) grain size and β fraction.

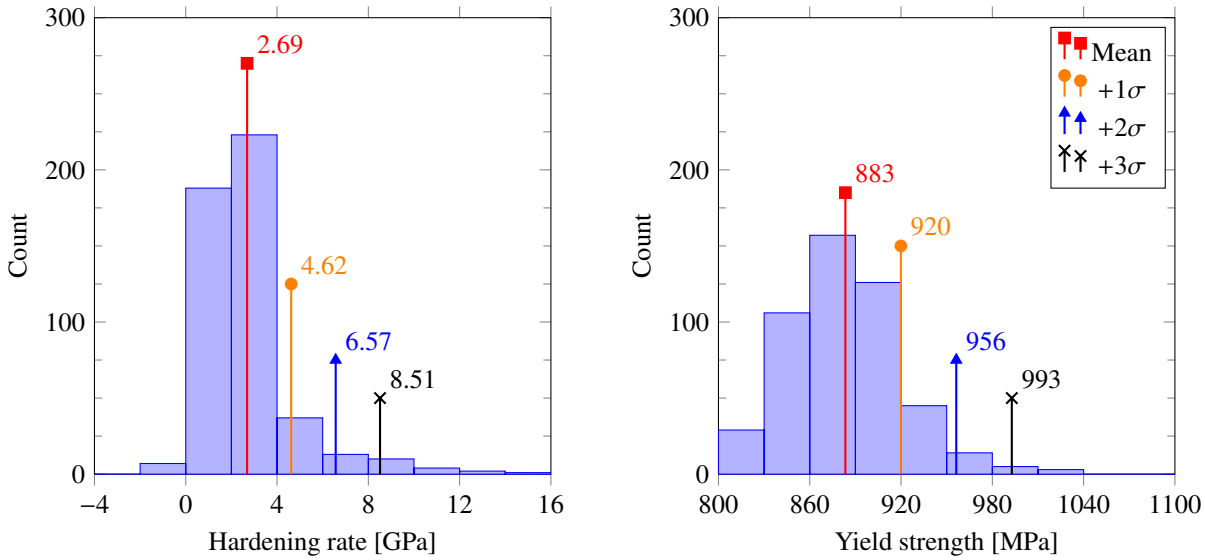

(a) (b)

Figure 3.5: Histograms for data distribution of (a) hardening rate and (b) yield strength. Flags used to show mean and standard deviations of data.

hardening rate to desired values.

Using the information shown in Figures 3.6c and 3.6d we can further examine the effect of grain size on the output yield strength and hardening rate. According to the output of the simulations, the grain size has little effect on the yield strength until the upper limit of 30 μm was reached. For these specific samples, increasing the β fraction had a stronger positive correlation than in samples with more grains. This trend also exists for the measured hardening rate, as the samples with the fewest grains show a significantly stronger correlation between hardening rate and β fraction. From these two plots it appears grain size has a minimal effect on yield strength and hardening rate at least for a fixed simulation volume (2.7×10^{-14} m^3 in our case).

3.3.2 Machine Learning Results

Prior to model fitting we investigated the relative importance of the feature variables. Feature importance measurement is similar to traditional forms of sensitivity analysis wherein

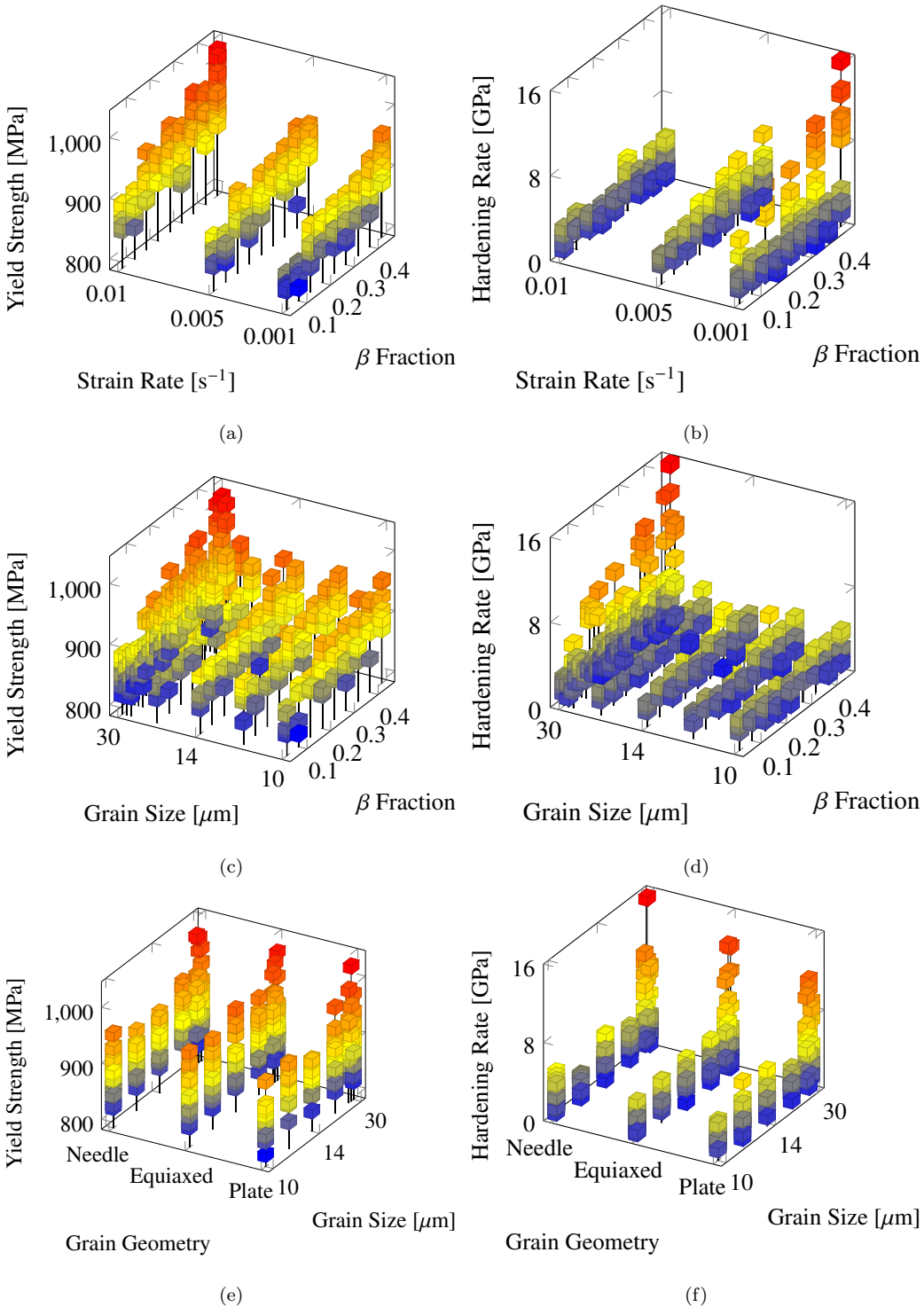

Figure 3.6: Yield strength and hardening rate plots versus multiple input parameters

the emphasis is typically on identifying which features have the most/least impact on the predicted variable. To do this we trained a random forest regressor and calculated the permutation importance for all features. A random forest was chosen to run the preliminary analysis because they have proven to be successful at adapting to a diverse set of problems [137]. The authors refer to the appendix and the attached works for a more thorough description of the regression technique. The permutation importance is calculated by randomly permuting the row-wise order of a given feature and then re-calculating the prediction scoring (RMSE, in this case) of the entire set [138, 139]. This procedure is done individually for all features and the normalized relative importance values are assigned based on the magnitude of decrease in the scoring for the permuted feature whereby the sum of all importance values is 1. The feature with the highest permutation importance decreases the prediction accuracy the greatest (of the feature variables) when its values are randomly permuted. The calculation of permutation importance is a common method to down-select from a high-dimensional feature set [140, 141]. The relative permutation importance values for both the yield strength and hardening rate models are given in Figure 3.7. For both models the grain geometry is the feature with the least importance (with values of 0.001 and 0.02 for the strength and hardening rates, respectively). All models were trained with the grain geometry feature both included and excluded and the better-performing model was selected. Excluding the grain geometry parameter increased the accuracy of all strength models and raised the average R^2 by 4%. For the hardening rate models the R^2 score increased by an average of 6%.

The skew of the hardening rate and yield strength outputs, 2.56 and 0.60 respectively, were initially considered as detrimental factors to both models' performances. However, re-training with normalized outputs did not meaningfully improve any of the models' behavior. Similarly the 3σ rule was applied to remove outlying data but model performance worsened across the board. During training all continuous features were normalized and the grain geometry feature was one-hot encoded (i.e. equiaxed=1, plate=0, needle=-1). Hy-

perparameter tuning was performed using 5-fold cross-validation and a grid search method.

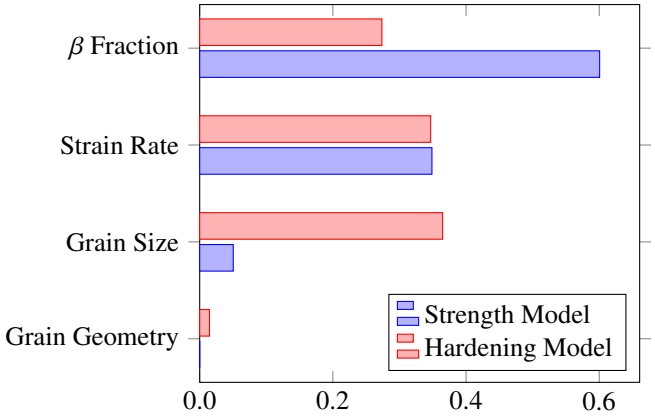

Figure 3.7: Feature importance as calculated by feature permutation with the trained random forest regression model. The *strength model* and *hardening model* correspond to the preliminary random forest regression models trained on the yield strength and hardening rate data, respectively.

The fitting results for the yield strength-predicting ML models is listed in Table 3.4, while Figure 3.8 plots the RMSE, MAE, and R^2 results for the testing data as well as the random dataset. All models have R^2 of 0.7 or below. The linear models (LR,R-LR) have performed similarly with R^2 values of 0.59 while the other four models (RFR, RFR, XGB, GB-R, ANN) have R^2 values of 0.64 to 0.70. The KNNR method fell in between the two regions with a R^2 value of 0.60. The poor relative performance of the linear models (LR, R-LR) is expected because the strength-microstructure relationships tend to be nonlinear.

The fitting results for the hardening rate-predicting ML models are given in Table 3.5, and the associated testing RMSE, MAE, and R^2 values are plotted in Figure 3.9. Again the non-linear models (KNNR, RT, RFR, XGB, GB-R, ANN) outperform the linear models (LR, R-LR). The hardening rate predictors do not perform as well as the yield strength predictors and the best hardening rate model (in terms of R^2) is RFR with R^2=0.62.

The distribution of true and predicted values for the the test evaluation of both the regularly-spaced and random datasets for several models are provided in Appendix 3.D.

Model	RMSE Test	MAE Test	R^2	RMSE Random
LR	22.3	17.3	0.59	25.4
R-LR	22.3	17.3	0.59	25.3
KNNR	21.4	16.7	0.62	24.8
RT	20.0	15.7	0.67	29.9
RFR	19.6	15.3	0.68	25.4
XGB	19.2	15.3	0.70	25.3
GB-R	19.3	15.2	0.69	25.6
ANN	20.8	15.6	0.64	24.8

Table 3.4: Model performance for predicting yield strength values. RMSE and MAE values are units of MPa.

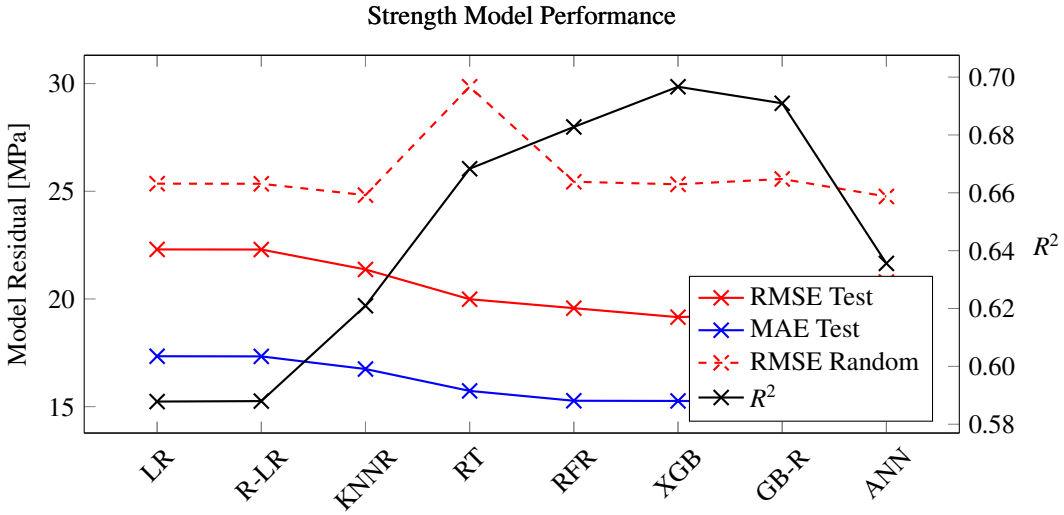

Figure 3.8: Performance of the models trained for fitting the strength data. Computed using a randomly selected test set of 100 samples.

Model	RMSE Test	MAE Test	R^2	RMSE Random
LR	1.78	1.26	0.10	1.08
R-LR	1.78	1.24	0.10	1.07
KNNR	1.13	0.86	0.59	1.34
RT	1.12	0.82	0.60	1.44
RFR	1.10	0.81	0.62	1.38
XGB	1.16	0.85	0.57	1.29
GB-R	1.17	0.87	0.57	1.36
ANN	1.34	0.86	0.47	1.16

Table 3.5: Model performance for predicting hardening rates. RMSE and MAE values are in units of GPa.

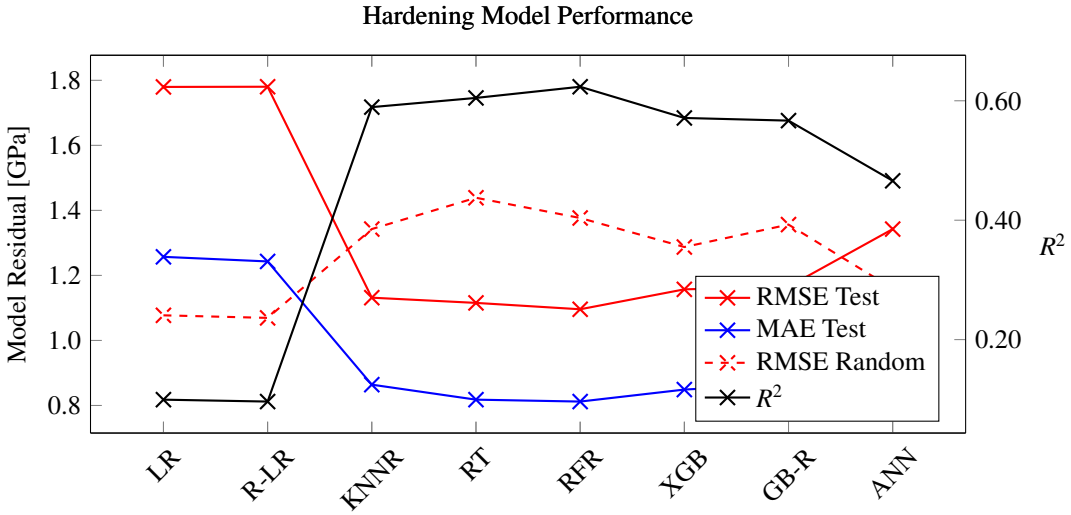

Figure 3.9: Performance of the models trained for fitting the strength hardening data. Computed using a randomly selected test set of 100 samples.

Figure 3.10 plots the target output of all unique points in the parametric space ordered from least to greatest for yield strength and hardening rate. The noise to signal ratio, $\sigma/\bar{x}$, is overlaid for each plot as red points. The σ values are the standard deviation of the four replica simulations run for each point and the $\bar{x}$ value is the mean that was used for model training. For the yield stress the signal to noise ratio is consistent for all points at values between 0.02 to 0.08. In contrast, the signal to noise ratio for the hardening rate data reaches values as high as 8.0 for the lowest hardening rate samples and and has an average value of approximately 1.0. The comparatively high $\sigma/\bar{x}$ value for the hardening rate data indicates that the hardening rate replicas had poor agreement with one another. Statistical variation in the target values is not a detriment to the microstructural model. Rather, it is expected that the random sampling construction procedure generates a unique microstructure for each simulation and certain micromechanical responses (e.g., hardening rate) are more sensitive to the stochastic nature of the construction than others. A detailed investigation of these parameters is beyond the scope of this paper and will be investigated in future work.

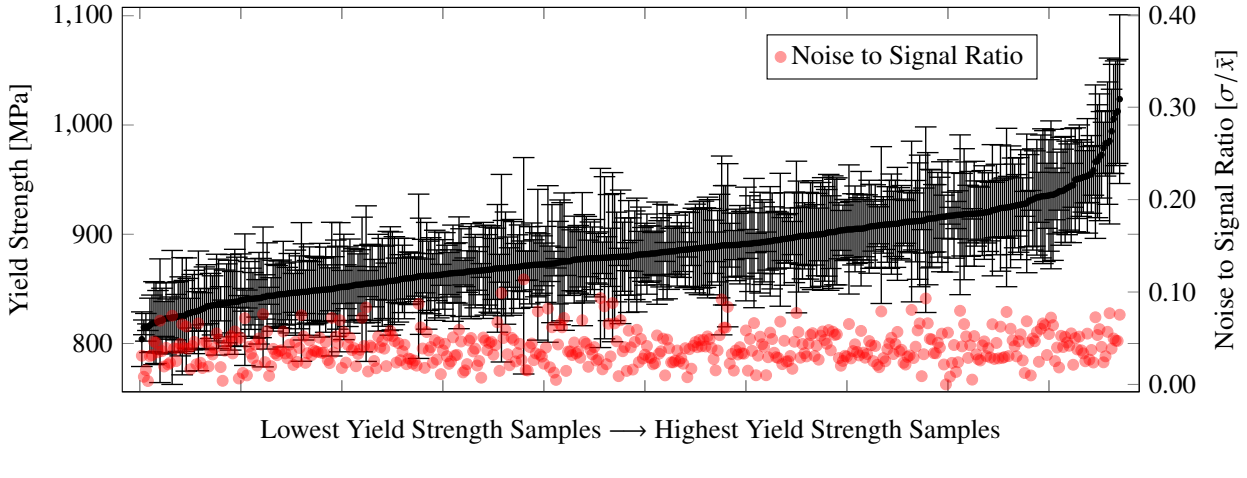

(a)

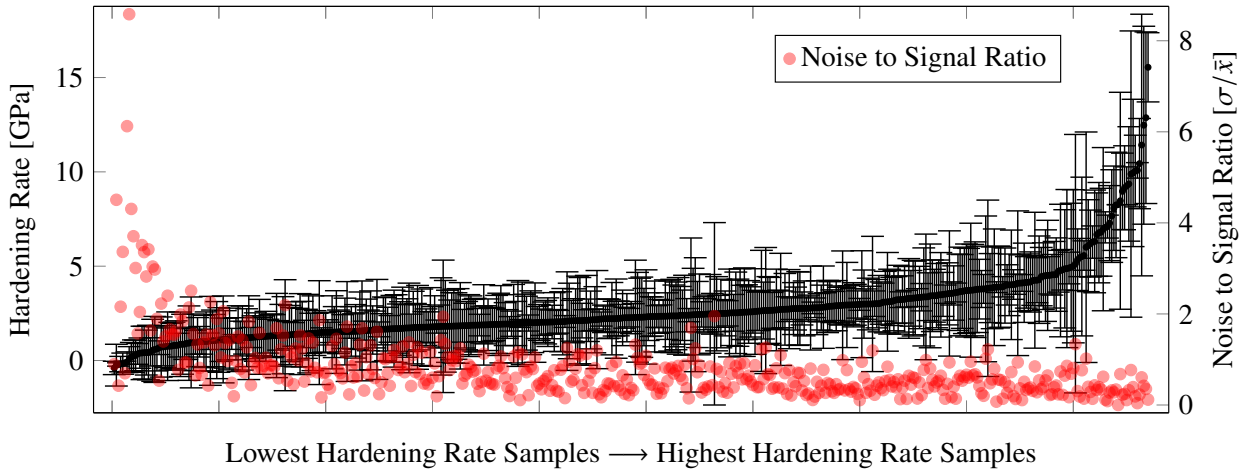

(b)

Figure 3.10: Plot of the mean target value from a unique point in simulation space ordered from least to greatest in terms of (a) yield strength and (b) hardening rate. Error bars are the standard deviation from 4 replicas simulated at each point. The red circles are the noise to signal ratio $\sigma/\bar{x}$.

Further understanding of the performance can be determined with the evolution of pairwise correlations between the feature variables and the target variables based on the number of simulations conducted. This provides information on how many simulations are needed before the model reaches a maximum in accuracy for each individual correlation value. This also provides information about the change in the correlation values, and how many simulations are needed before reliable information can be obtained from the simulated data

set. Figure 3.11 shows the Pearson correlation coefficient versus the number of unique data points simulated for both yield strength and hardening rate based on the four input parameters. As the figure shows, convergence in the predictors is achieved after 200 samples approximately. The yield strength plot confirms the positive correlation from β fraction and strain rate, and the minimal correlation with grain size and geometry. The hardening rate plot shows the near-zero positive correlation from β fraction and geometry, and the negative correlation from grain size and strain rate.

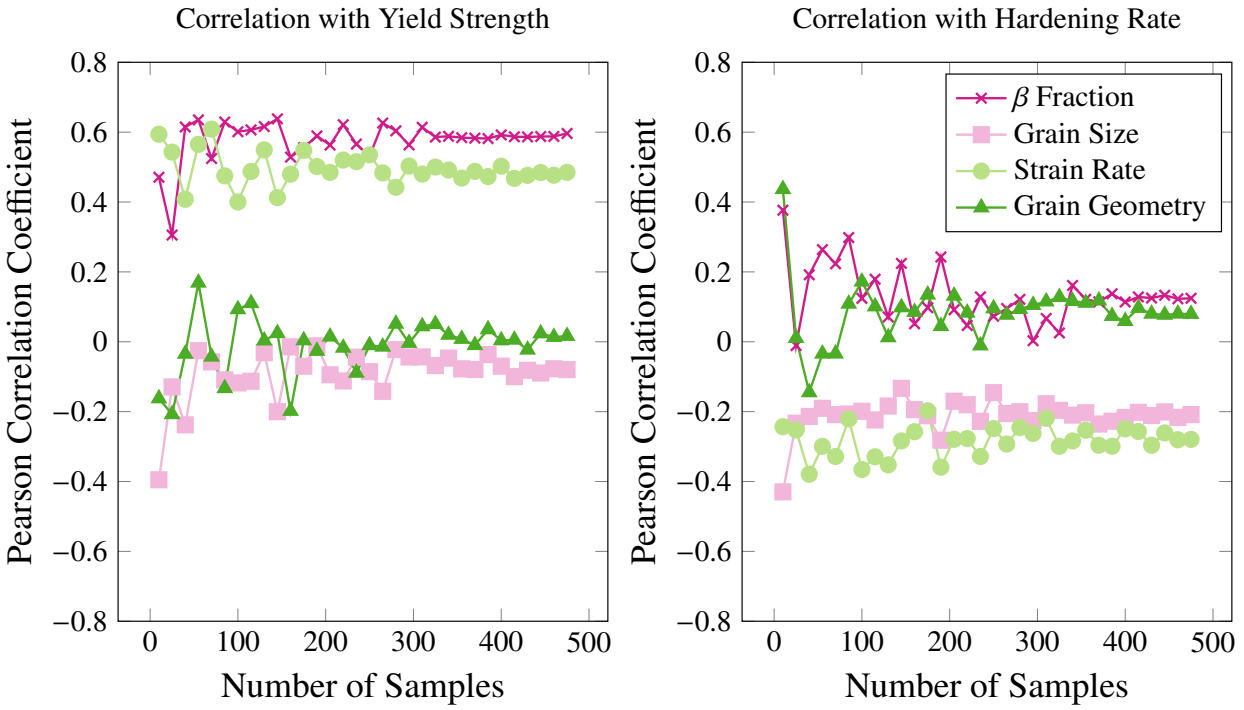

(a) (b)

Figure 3.11: Pearson correlation coefficient versus number of samples for (a) yield strength and (b) hardening rate.

3.4 Discussion

The main purpose of this study is to demonstrate how a relative large parameter set (defined by four microstructural variables, with several values each, 567 distinct simulation conditions

in total) can be parsed effectively using machine learning techniques to predict useful outcomes in terms of alloy mechanical properties. Ultimately, studies such as the present one are aimed at improving and refining the alloy design process to save scarce resources, both in terms of time and money, and accelerate material characterization and synthesis by focusing on parameters with the greatest influence. Specifically, we have chosen a system with a relatively complex microstructure but great metallurgical promise, namely Ti-6Al-4V alloys with various features. Indeed, Ti-6Al-4V has recently been the subject of design optimization efforts using machine learning techniques [142, 143]. Next, we discuss our main findings and identify the lessons learned and their potential applicability.

3.4.1 Plasticity Model Discussion

The constitutive law and flow rule used in this work have been chosen due to their simplicity so that –in principle– they lead to uncomplicated material responses to facilitate the extraction of trends using the machine learning methods. However, they are still grounded on solid crystal plasticity principles and some interesting results are worth being discussed.

For example, the yield stress displays near-logarithmic growth with strain rate for β fractions up to roughly 30% vol, as shown in Fig. 3.13a This agrees well with previous Ti-6Al-4V studies [122, 123, 144] and accurately reflects the basis of a flow stress power law. When the β fraction is greater than 30%, the σ_y-$\dot{\varepsilon}$ relationship transitions to being exponential. The amount of β in the crystal plays an increasingly important role in determining the magnitude of the yield strength as $\dot{\varepsilon}$ is increased (see Figure 3.6b). The β fraction and σ_y relationship is near linear which agrees with previous works [145] and should be expected as a function of the general rule of mixtures. This is demonstrated in Fig. 3.13b. In a similar study of Ti-6Al-4V deformed dynamically (at rates larger than those considered here), the slopes of the β fraction and σ_y relation were observed to increase with strain rate [145]. In the crystal plasticity model employed here, neither phase displays intrinsic hardening (recall that $k_2 = 0$ for both the α and β phases in Table 3.1). Thus, the sole source of hardening is

given by the value of the resolved shear stress itself, which as a general rule is always higher for systems with a reduced number of slip systems (and the associated lattice stress). As indicated in Tables 3.6 and 3.7, the HCP α phase contains a total of 39 independent slip systems, against the 12 of the BCC β phase. It is thus reasonable to obtain an increase in the hardening rate as the volume fraction of β increases.

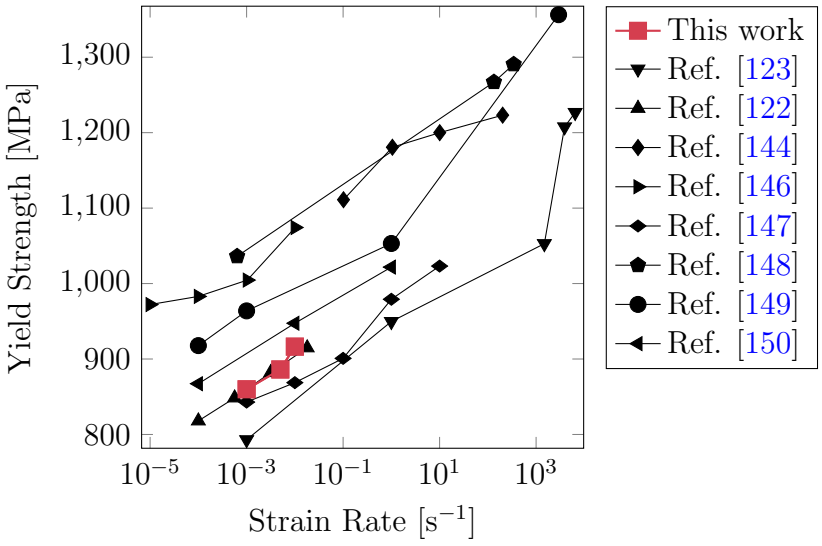

Figure 3.12: Yield strength as a function of strain rate for this study and experimentally determined values from literature.

Regarding grain geometry, in this study it was seen to have practically no effect on the measured yield strength or hardening rate, as shown in Figs. 3.6e and 3.6f. Grain geometry effects may have been minimized due to the choice to simulate lamellae with minimal microstructural texture, as opposed to adding texture as another input parameter and expanding the parameter space. Though each α or β layer had its own unique orientation, there was no difference in interlayer misorientation between the needle, equiaxed, and plate geometries. Thus each grain geometry resulted in low texture crystals that differed in grain shape but conserved grain boundary area and texture. This negates the anisotropy of the HCP phase, making the simulation volume directionally-independent. This may also explain the presence of outliers in the simulations with larger grain sizes (25-30 μm) as fewer grains may randomly be oriented in harder or softer directions. Though beyond the scope of this

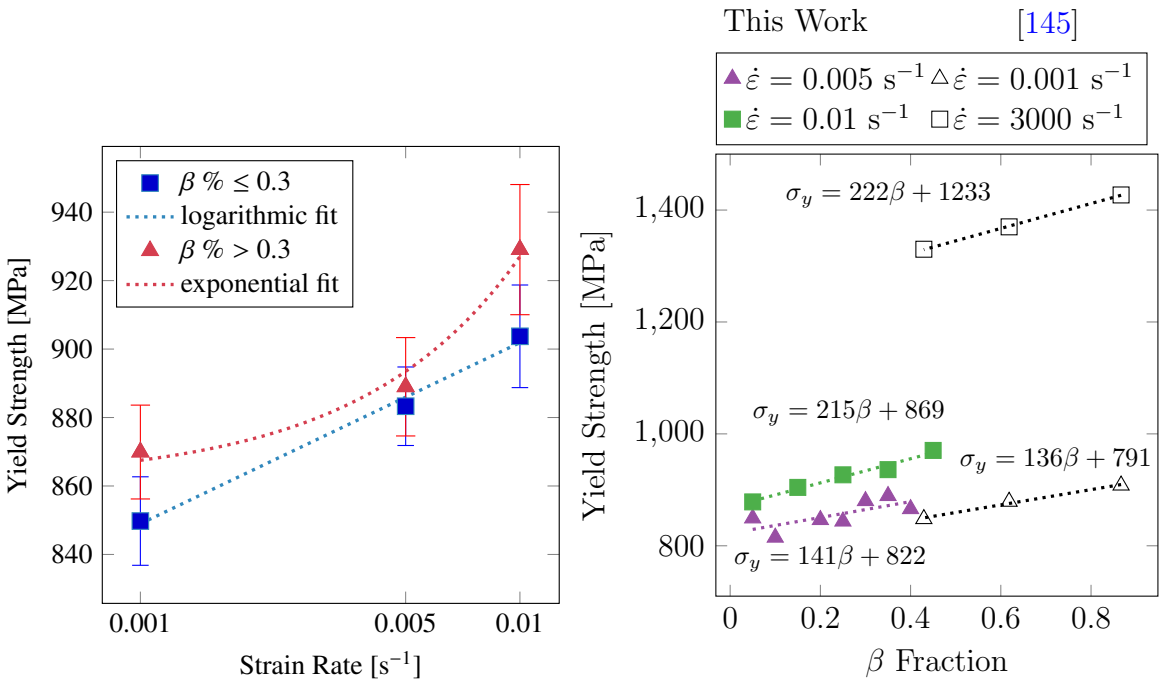

(a) (b)

Figure 3.13: (a) A subset of the data partitioned by crystals with β % $\leq$ 0.3 (in blue) and β % > 0.3 (in red). The crystals with β % $\leq$ 0.3 have a logarithmic relationship between σ_y and $\dot{\varepsilon}$. Meanwhile the crystals with β % > 0.3 follow an exponential trend for σ_y and $\dot{\varepsilon}$ for the range explored. (b) Yield strength as a function of β fraction for a subset of $\dot{\varepsilon} = 0.005$ s^{-1} and $\dot{\varepsilon} = 0.01$ s^{-1} data plotted alongside data from [145].

work, this effect can be corrected by sampling lamellar packets that are constructed with preferential orientations that consider the grain shape and orientation itself. This type of adjustment could then provide insight to the difference in mechanical response provided by plate, needle, and equiaxed structures with lamellar and non-lamellar substructures that are oriented different ways within the outer grain structures.

The yield strength data produced in this study deviates from the classical Hall-Petch relationship (see Figure 3.6c) when the dislocation mean free path is considered to be the grain size. The limited influence of grain size on the strength and hardening is likely a result of the lamellar substructure. Since the lamellae packing does not differ in terms of spacing or density between large/small grains the total inter-lamellar distance remains roughly constant despite variations in the grain size (for the range explored). This effect could be mitigated by imposing a local hardening condition that is reflective of the dislocation pileup due to the true grain size of local lamellae packet. Alternatively a non-lamellar substructure (i.e., large α and β grains) or Hall-Petch-type strengthening parameter could be used.

Furthermore, is has been experimentally observed that the α/β lamellar thickness and ratio in Ti-6Al-4V strongly dictates mechanical behavior [151–155]. It is possible that negligible influence of grain size may, rather, be due to the α/β lamellae width effects having a dominant influence on strength. Figure 3.14 shows the yield strength as a function of lamellar spacing and α lamellae width for this study and experimental data found in literature. Note that since we used constant lamellae packet size (i.e., the width of a single α/β bilayer) there is a single data point from this work in Figure 3.14a. The Hall-Petch type relationship is recovered for yield strength when the dislocation free glide distance is considered to be the α lamellae width, as shown in Figure 3.14b. Considering that BCC β phase is generally softer than the HCP β phase (see Figure 3.1b), increasing the β content would be expected, to first order, to lead to a decrease in strength. However, here we see that the Hall-Petch strengthening achieved through the reduction in the α lamellae widths more than compensates and increases the strength of the alloy. Future work will include

refinement of the lamellar spacing/grain size relationship in the context of the dual-phase CPFE model.

Further improvements can be made to the model by incorporating mechanisms such as grain boundary strengthening, reinforcement particle strengthening, precipitation/solid solution strengthening, and temperature effects by modifying the crystal strength and plasticity expressions (equations 3.6-3.8). Consideration of non-lamellar microstructures and dynamic loading effects may be beneficial to assist with modeling high-strain rate phenomena.

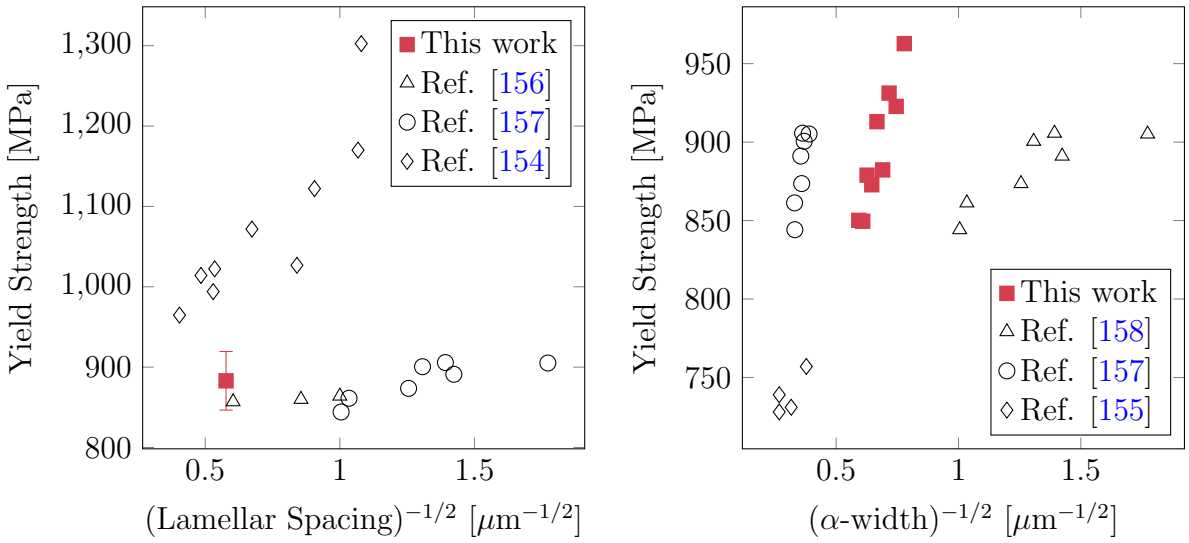

Figure 3.14: Yield strength as a function of (a) lamellar spacing and (b) α width for this study and experimentally determined values from literature. Lamellar spacing is considered the width of a combined α/β bilayer.

3.4.2 Machine Learning Discussion

Multidimensional parametric design spaces can be complex to analyze by 'hand' and are further complicated by non-linear feature behavior. To aid with analysis of these types of design spaces the ultimate goal of many machine learning regression exercises is to provide a predictive model for target values learned through example data. In this case, the regression exercise was aimed at modeling the yield strengths and hardening rate of a dual-phase Ti

crystal with certain microstructural traits. Several models were trained for both target values using a uniformly-spaced dataset and then evaluated using both the uniform grid and random dataset. An ensemble regressor was constructed from all the trained models [159]. An ensemble regressor makes a prediction based off of the weighted average of individual predictions from several multiple models. In our case, the weight prescribed to each model was calculated using the arbitrary expression:

$$w_i = \frac{1}{3}\left[\left(\frac{\mathrm{RMSE}^i_{\mathrm{test}}}{\sum \mathrm{RMSE}^i_{\mathrm{test}}}\right)^{-1} + 2\left(\frac{\mathrm{RMSE}^i_{\mathrm{random}}}{\sum \mathrm{RMSE}^i_{\mathrm{random}}}\right)^{-1}\right] \tag{3.15}$$

where $\mathrm{RMSE}^i_{\mathrm{test}}$ and $\mathrm{RMSE}^i_{\mathrm{random}}$ are the testing root-mean-squared errors calculated using the test and random datasets, respectively. Because true microstructural traits exist on a continuum scale, we placed an additional (arbitrary) weight on the performance of the models on the random dataset. Predicted yield strength and hardening rate values as a function of the β fraction and grain size from the voting models are given in Figure 3.15. Though it is beyond the scope of this study, the authors note that the influence of randomly sampled data on an otherwise uniformly distributed parametric dataset is an interesting premise for improving a model's predictive power. That is, how much "non-grid" data should be added to an otherwise organized dataset in order to achieve an acceptably generalized model.

Lastly, it is important to recognize that the predictive power of the models could undoubtedly be improved with more data. Increasing the number of replicas at each point in parametric space would help further reduce the noise to signal ratio, particularly for the hardening rate data. This is evidenced by Figure 3.16 which shows the average signal to noise ratio as a function of the number of replicas. 100 structures were selected at random to generate a fifth replica. Similarly the models would benefit from a "finer gridded" parametric space (e.g., simulating structures with $\dot{\epsilon} = 0.0075$ s^{-1}, $\dot{\epsilon} = 0.002$ s^{-1}) that would simply provide a more rich training set.

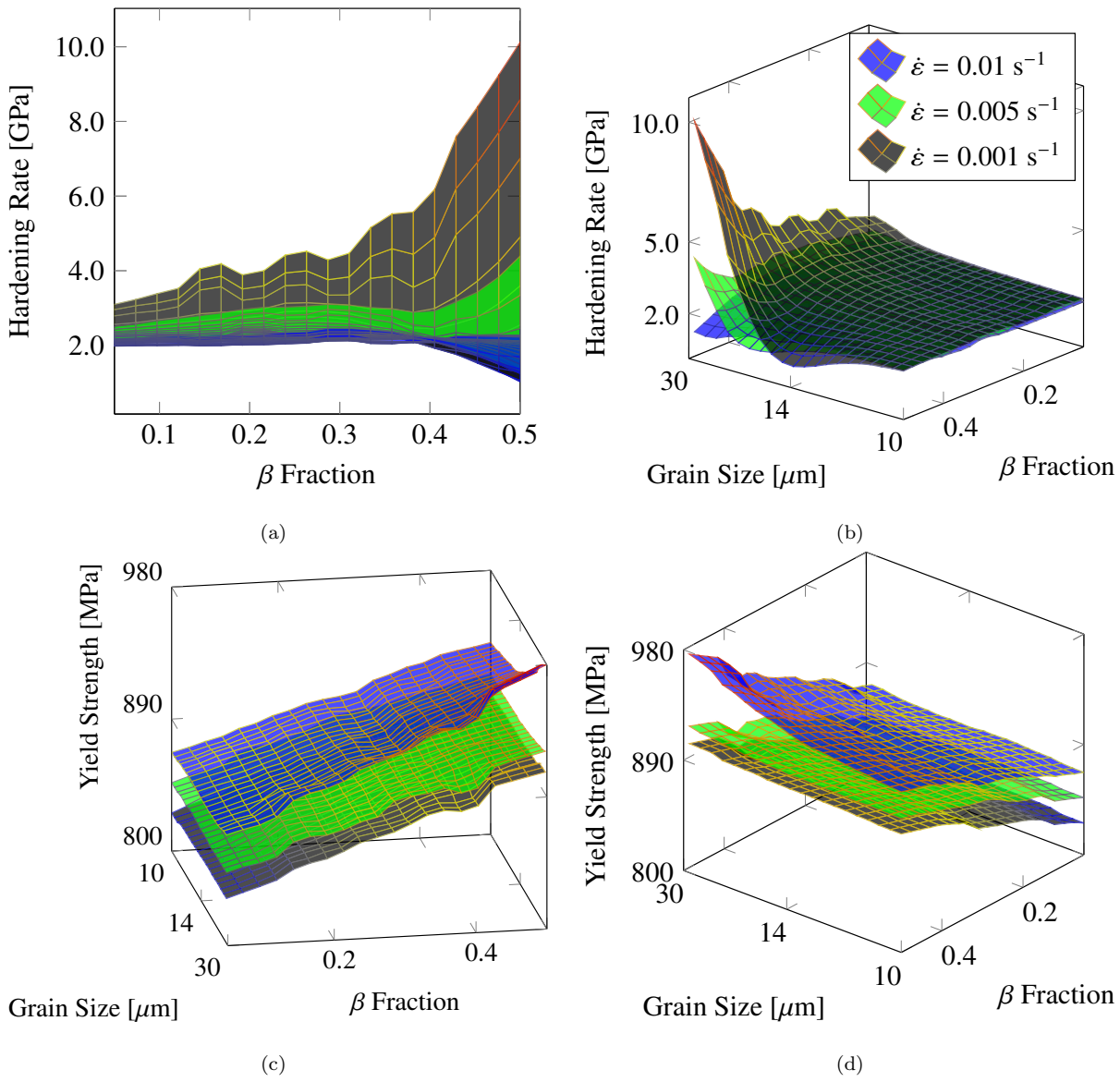

Figure 3.15: Predictions of (a)-(b) hardening rate and (c)-(d) yield strength as a function of grain size and β fraction for weighted voting regressor. Each plot contains three planes are plotted in black, green, and blue that correspond to $\dot{\epsilon}$ values of 0.001, 0.005, and 0.01 s^{-1}, respectively.

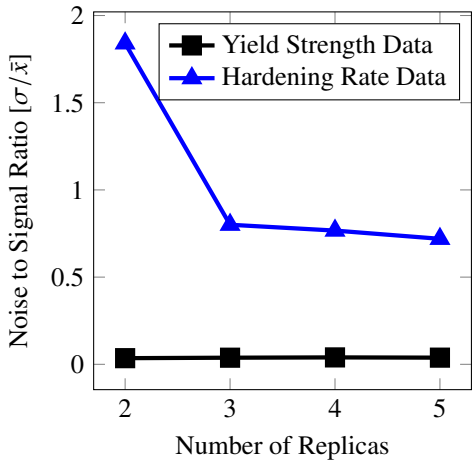

Figure 3.16: Noise to signal ratio as a function of the number of replicas for the yield strength and hardening rate data

3.5 Conclusions

We conclude the paper with our most important findings:

- We have extended a single-crystal plasticity model to study a polycrystal dual phase material with complex microstructures. The model captures dual-phase BCC/HCP microstructures using standard dislocation evolution models with features inspired in experimental behavior.

- Our model agrees with the tensile testing behavior observed in other works and does well to capture trends in crystal strength.

- Several machine learning regression models were trained on the data to produce ensemble models that can make quick predictions and generalize the yield strength and hardening rate CPFE outputs.

- We demonstrated clear trends in yield strength and hardening rate as a function of β fraction, strain rate, grain geometry, and grain size.

- As general conclusions, (i) the grain shape has practically no bearing on yield strength and hardening rate outcomes, (ii) the β-phase volume fraction was seen to be the most

influential feature on both outcomes, (iii) strain rate is a strong predictor of yield strength but not of hardening rate, while grain size is weakly and negatively correlated with yield strength and hardening, respectively.

- Future work will be aimed at extending the plasticity model to include temperature, obstacles, and dynamic loading conditions.

3.A Finite Element Implementation

The finite element implementation in `COMSOL5.5` for this study is fully described in [61]. A MUMPS direct solver and BDF (Backward Differential Formula) time stepping algorithm were employed. All simulations were performed with a free tetrahedral mesh with 99883 elements and 595620 degrees of freedom. The stiffness matrices for the α and β phases have been taken from refs.[160–162] and are given below (all values in GPa).

$$\mathcal{C}^{\alpha} = \begin{bmatrix} 169.4 & 90.0 & 66.0 & 0 & 0 & 0 \\ 90.0 & 169.4 & 66.0 & 0 & 0 & 0 \\ 66.0 & 66.0 & 169.2 & 0 & 0 & 0 \\ 0 & 0 & 0 & 7.4 & 0 & 0 \\ 0 & 0 & 0 & 0 & 7.4 & 0 \\ 0 & 0 & 0 & 0 & 0 & 46.8 \end{bmatrix}$$

$$\mathcal{C}^{\beta} = \begin{bmatrix} 119.4 & 55.7 & 55.7 & 0 & 0 & 0 \\ 55.7 & 119.4 & 55.7 & 0 & 0 & 0 \\ 55.7 & 55.7 & 119.4 & 0 & 0 & 0 \\ 0 & 0 & 0 & 31.9 & 0 & 0 \\ 0 & 0 & 0 & 0 & 31.9 & 0 \\ 0 & 0 & 0 & 0 & 0 & 31.9 \end{bmatrix}$$

The CP model admits slip on basal, prismatic and pyramidal planes for the α phase (3, 11,

Table 3.6: Conversion from 4-index slip system to 3-index notation

slip system type	No.	slip plane		slip direction	
		4-index	3-index	4-index	3-index
basal	1	(0001)	(001)	$[2\bar{1}\bar{1}0]$	[100]
	2	(0001)	(001)	$[\bar{1}\bar{1}20]$	$[\bar{1}\bar{1}0]$
	3	(0001)	(001)	$[\bar{1}2\bar{1}0]$	[010]
prismatic	4	$(01\bar{1}0)$	(010)	$[2\bar{1}\bar{1}0]$	[100]
	5	$(1\bar{1}00)$	$(1\bar{1}0)$	$[\bar{1}\bar{1}20]$	$[\bar{1}\bar{1}0]$
	6	$(\bar{1}010)$	$(\bar{1}00)$	$[\bar{1}2\bar{1}0]$	[010]
	7	$(01\bar{1}0)$	(010)	$[2\bar{1}\bar{1}3]$	[101]
	8	$(01\bar{1}0)$	(010)	$[2\bar{1}\bar{1}\bar{3}]$	$[10\bar{1}]$
	9	$(1\bar{1}00)$	$(1\bar{1}0)$	$[\bar{1}\bar{1}23]$	$[\bar{1}\bar{1}1]$
	10	$(1\bar{1}00)$	$(1\bar{1}0)$	$[\bar{1}\bar{1}2\bar{3}]$	$[\bar{1}\bar{1}\bar{1}]$
	11	$(\bar{1}010)$	$(\bar{1}00)$	$[\bar{1}2\bar{1}3]$	[011]
	12	$(01\bar{1}0)$	(010)	[0001]	[001]
	13	$(\bar{1}010)$	$(\bar{1}00)$	[0001]	[001]
	14	$(1\bar{1}00)$	$(1\bar{1}0)$	[0001]	[001]

and 25 slip systems respectively), and close-packed slip for the β phase (12 slip systems). All vectors $\boldsymbol{s}$ and $\boldsymbol{m}$ in eq. (3.3) for the hexagonal phase are expressed in three-component Miller notation using the conversion introduced by Frank [163]:

$$[h\ k\ i\ l] \rightarrow [(h-i)\ (k-i)\ l] \tag{3.16}$$

$$(h\ k\ i\ l) \rightarrow (h\ k\ l) \tag{3.17}$$

These expressions satisfy the orthogonality relations between slip direction and slip plane normal. The slip systems considered in this work are given in Tables 3.6 and 3.7.

The slip systems for BCC crystals capture $^1/_2\langle 111\rangle\,\{110\}$ and are given in past publications by our group [164, 165].

Table 3.7: Conversion from 4-index slip system to 3-index notation

slip system type	No.	slip plane		slip direction	
		4-index	3-index	4-index	3-index
pyramidal	15	$(01\bar{1}1)$	(011)	$[2\bar{1}\bar{1}0]$	$[100]$
	16	$(0\bar{1}11)$	$(0\bar{1}0)$	$[2\bar{1}\bar{1}0]$	$[100]$
	17	$(1\bar{1}01)$	$(1\bar{1}1)$	$[\bar{1}\bar{1}20]$	$[\bar{1}\bar{1}0]$
	18	$(\bar{1}101)$	$(\bar{1}11)$	$[\bar{1}\bar{1}20]$	$[\bar{1}\bar{1}0]$
	19	$(\bar{1}011)$	$(\bar{1}01)$	$[\bar{1}2\bar{1}0]$	$[010]$
	20	$(10\bar{1}1)$	(101)	$[\bar{1}2\bar{1}0]$	$[010]$
	21	$(\bar{1}011)$	$(\bar{1}01)$	$[2\bar{1}\bar{1}3]$	$[101]$
	22	$(\bar{1}101)$	$(\bar{1}11)$	$[2\bar{1}\bar{1}3]$	$[101]$
	23	$(\bar{2}112)$	$(\bar{2}12)$	$[2\bar{1}\bar{1}3]$	$[101]$
	24	$(10\bar{1}1)$	(101)	$[2\bar{1}\bar{1}\bar{3}]$	$[10\bar{1}]$
	25	$(1\bar{1}01)$	$(1\bar{1}1)$	$[2\bar{1}\bar{1}\bar{3}]$	$[10\bar{1}]$
	26	$(2\bar{1}\bar{1}2)$	$(2\bar{1}2)$	$[2\bar{1}\bar{1}\bar{3}]$	$[10\bar{1}]$
	27	$(10\bar{1}1)$	(101)	$[\bar{1}\bar{1}23]$	$[\bar{1}\bar{1}1]$
	28	$(01\bar{1}1)$	(011)	$[\bar{1}\bar{1}23]$	$[\bar{1}\bar{1}1]$
	29	$(11\bar{2}2)$	(112)	$[\bar{1}\bar{1}23]$	$[\bar{1}\bar{1}1]$
	30	$(\bar{1}011)$	$(\bar{1}01)$	$[\bar{1}\bar{1}2\bar{3}]$	$[\bar{1}\bar{1}\bar{1}]$
	31	$(0\bar{1}11)$	$(0\bar{1}1)$	$[\bar{1}\bar{1}2\bar{3}]$	$[\bar{1}\bar{1}\bar{1}]$
	32	$(\bar{1}\bar{1}22)$	$(\bar{1}\bar{1}2)$	$[\bar{1}\bar{1}2\bar{3}]$	$[\bar{1}\bar{1}\bar{1}]$
	33	$(1\bar{1}01)$	$(1\bar{1}1)$	$[\bar{1}2\bar{1}3]$	$[011]$
	34	$(0\bar{1}11)$	$(0\bar{1}1)$	$[\bar{1}2\bar{1}3]$	$[011]$
	35	$(1\bar{2}12)$	$(1\bar{2}2)$	$[\bar{1}2\bar{1}3]$	$[011]$
	36	$(\bar{1}101)$	$(\bar{1}11)$	$[\bar{1}2\bar{1}\bar{3}]$	$[01\bar{1}]$
	37	$(01\bar{1}1)$	(011)	$[\bar{1}2\bar{1}\bar{3}]$	$[01\bar{1}]$
	38	$(\bar{1}101)$	$(\bar{1}11)$	$[\bar{1}2\bar{1}\bar{3}]$	$[01\bar{1}]$
	39	$(\bar{1}2\bar{1}2)$	$(\bar{1}22)$	$[\bar{1}2\bar{1}\bar{3}]$	$[01\bar{1}]$

3.B Construction of Dual Phase Lamellar Polycrystals

All grains were constructed as Voronoi tessellations wherein grain centers c_j were randomly selected from a cubic grid and each individual point p_i was assigned to the nearest grain center such that:

$$p_i^g = \min\left(\text{dist}(p_i, c_j) : j \in \{1, ..., C\}\right) \tag{3.18}$$

where p_i^g is the grain assignment for the point p_i. Here there are a total of C grain centers and the function $dist(p_i, c_j)$ returns the distance between the grid point p_i and the grain center c_j. The distance equation is a modified euclidean distance function give as:

$$\text{dist}(p_i, c_j) = \left(\frac{p_i^x - c_j^x}{sx}\right)^2 + \left(\frac{p_i^y - c_j^y}{sy}\right)^2 + \left(\frac{p_i^z - c_j^z}{sz}\right)^2 \tag{3.19}$$

where sx, sy, and sz are distance scaling factors that enable elongated grains. For this study the scaling factors for the equiaxed, plate, and needle grains are given in Table 3.8. To achieve a unique lamellar structure within each grain a set of plate-like grains are first

Grain Geometry	sx	sy	sz
Equiaxed	1	1	1
Needle	1	1	4
Plate	1	4	4

Table 3.8: Grain geometry parameters.

constructed. Grains are assigned to either α or β phase as a function of their the distance from the x-axis such that:

$$c(j) = \begin{cases} \beta \text{ phase}, & \text{if } F_\beta/G \leq \min\left(\left|L_j - nl\right| : n \in \{0, ..., G+1\} \text{ where } G = \left\lfloor H/l \right\rfloor\right) \\ \alpha \text{ phase}, & \text{otherwise} \end{cases} \tag{3.20}$$

here L is the x coordinate of the grain center, l is the spacing between same-phase lamellae, F_β is the β phase fraction out of 100, and H is the total height of the simulation cube. The

$G = \lfloor H/l \rfloor$ term indicates the number of lamellae layers in each simulated cube while the F_β/G term is the thickness of each β layer. Once a plate-like cube was constructed it was put through a set random rotations across the x, y, and z axis to achieve a unique grain alignment. For each simulation a set of 20 unique lamellar crystals were constructed and the sampled from to populate the grain geometry defined by the original Voronoi tesselations –ultimately leading to equiaxed, needle, or plate-like grain geometries with an intra-grain α/β lamellar structure.

We recognize that there are various forms of α/β subgrain morphologies but here we focus on lamellar structures for the purpose of this study.

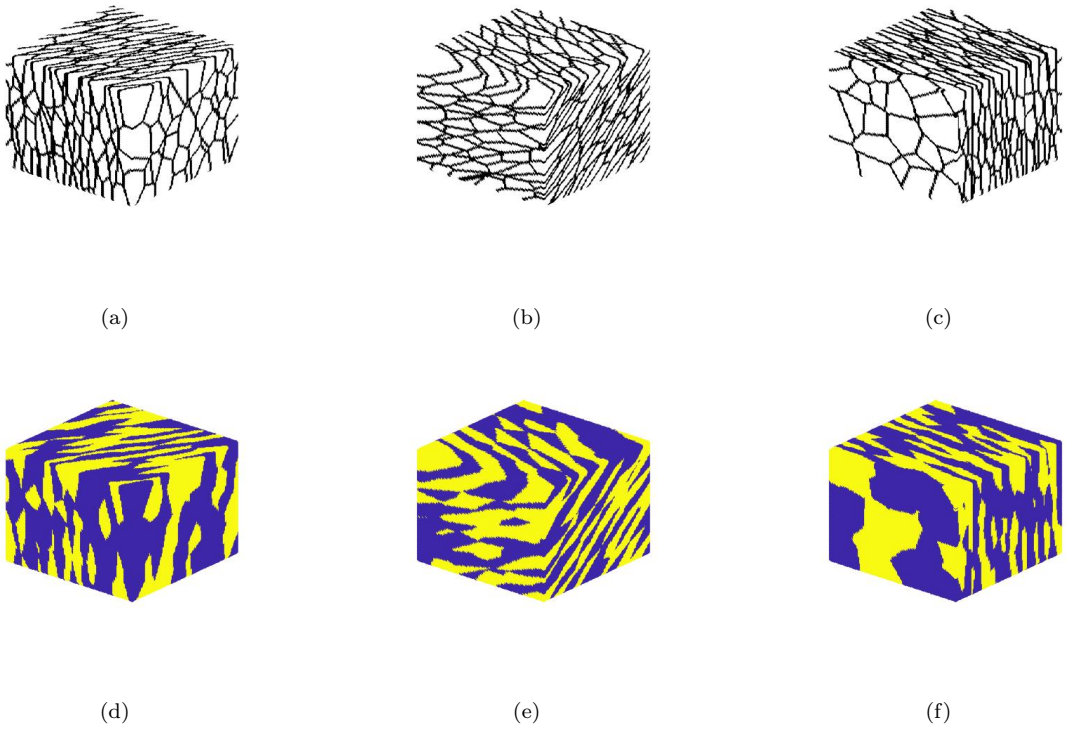

Figure 3.17: Pure lamellar crystals with (a)-(c) outlined phase boundaries and (d)-(f) shading indicating either α (blue) or β (yellow) phase. All crystals have been put through 3 random rotations across their x, y, and z axes.

3.C Machine Learning Regression Models

3.C.1 Linear Regression

Given the simple hypothesis function of:

$$f(\theta) = \theta_0 x_0 + \theta_1 x_1 + ...\theta_n x_n \tag{3.21}$$

where θ are the feature weights and x_n are the feature values for n features. Considering optimizing a least-squares cost function, a direct solution for the optimal θ values can be expressed as:

$$\theta_{LR} = \left(X^T X\right)^{-1} X^T y \tag{3.22}$$

where X is the collection of input features and y is the output values for each instance. The above expression does not hold for other cost functions, but rather, demonstrates the form of the model.

3.C.2 Ridge Linear Regression

To regularize the traditional linear regression expression in equation 3.22 a complexity penalty of $\lambda \sum_{i=1}^{n} \theta_j^2$ can be added to the least-squares cost function. Because the cost function is still convex, there is a unique solution:

$$\theta_{RR} = \left(X^T X + \lambda I\right)^{-1} X^T y \tag{3.23}$$

where $\lambda \in [0, \infty)$ is the regularization parameter and I is the identity matrix.

3.C.3 K-Nearest Neighbors Regression

K-nearest neighbors is a non-parametric method that that approximates the value of a new instance by averaging the target value of observations in the same neighborhood. Given a new instance, an estimate is calculated by first finding the K-nearest neighbors in Euclidean

space and then averaging the feature set such that:

$$y_i = \frac{1}{k} \sum_{j=1}^{k} y_j w_j \tag{3.24}$$

where k is the number of nearest neighbors, y_j is the target value of neighbor j, and w_j is a distance-related weight. The k parameter is typically learned during training.

3.C.4 Regression Tree

Building a decision tree can be thought of as recursively applying the process of dividing a single parent node into its two child nodes. As such, the process for the division of one node can be used to fully define the construction process. To find the data points that will be allocated between the two child nodes the optimal data partition is selected such that the sum of squares is minimized between the creation of the two new nodes, otherwise expressed as:

$$\arg\min \sum_{i=1}^{j} \sum_{k=1}^{N_i} (y_k - \bar{y_i})^2 \tag{3.25}$$

where i is a new node, j is the total number of new new nodes, k is a data point in the i partition, N_i is the total number of data points in the partition i, and $\bar{y_i}$ is the average target value of the instances in partition i. A greedy algorithm is commonly used to select the partitions. The size of the regression tree (e.g. width and depth) is typically set prior to construction and a full tree is built in the first pass. Estimations are made by taking the average target value of all data points in a terminal node. Variance and complexity reduction is then achieved by pruning of the full tree. One possible regression tree cost function can be given as:

$$C_\alpha(T) = \sum_{m=1}^{T} \sum_{k=1}^{N_m} (y_k - \bar{y_i})^2 + \alpha T \tag{3.26}$$

where α is a regularization parameter, N_m is the number of observations in terminal node m, and T is the number of terminal nodes. Minimization of equation 3.26 is achieved through collapsing nodes to achieve a sub-tree T such that $T \subset T_o$ where T_o is the full tree. The

weakest link approach to pruning is then commonly used: nodes are collapsed by order of least contribution to $C_\alpha(T)$ (i.e. lowest residual sum of squares error) such that a set of trees are produced that are gradually more generalized and can be fit to α.

3.C.5 Random Forest Regression

Random forest regression is an extension of regression trees that utilizes bootstrapping aggregation, that is, the aggregation of many "weak" regression trees into an ensemble model that is typically lower variance than its individual components. A random forest is constructed as:

1. For a training set of size n, set features X, and responses y, select β, the total number of trees in the forest.
2. Sample a subset of instances of the training data $X_t \subset X$, $y_t \subset y$ and train a new tree f_t on the data.
3. Repeat step 2 until β trees have been constructed.

To make an estimate using the random forest simply take the average prediction of all trees in the forest as:

$$\hat{f}(x^i) = \frac{1}{\beta} \sum_{i=1}^{\beta} f_t(x^i) \tag{3.27}$$

3.C.6 `XgBoost`

A complete mathematical description of `XgBoost` is beyond the scope of this work and a brief review is given here. `XgBoost` is an algorithm that applies the gradient tree boosting method. Gradient tree boosting takes advantage of both ensemble learners and iterative improvement to a model by means of using the residual loss of the previous iteration to train a new estimator. Estimators are added to the model such that the predicted result at

iteration t is:

$$\hat{y}_i^t = \hat{y}_i^{t-1} + f_t(x_i) \tag{3.28}$$

where $f_t(x)$ is the new estimator. In the case of `XgBoost`, the generalized objective function to optimize during each step can be given as:

$$\text{obj}^{(t)} = \sum_{j=1}^{T} \left(G_j w_j + \frac{1}{2} H_j w_j^2 \right) + \Omega_{\lambda\gamma}(T) \tag{3.29}$$

where Ω is a model complexity contribution that is a function of the model of all the trees T with regularization parameters λ and γ. The parameter w_j is the leaf weights, and G_j and H_j are the sum of the first and second order components of the Taylor expansion of the specified loss function for leaf j, respectively. From here, an expression for a measure of how "good" a tree structure $q(x)$ is can be written as:

$$\text{obj}^* = -\frac{1}{2} \sum_{j=1}^{T} \frac{G_j^2}{H_j + \lambda} + \gamma T \tag{3.30}$$

We can build a tree that continues to split nodes so long as the "goodness gained" from a given node split is larger than the regularization parameter γ, as:

$$\text{Gain} = \frac{1}{2} \left(\frac{G_L^2}{H_L + \lambda} + \frac{G_R^2}{H_R + \lambda} - \frac{(G_L + G_R)^2}{H_L + H_R + \lambda} \right) - \gamma \tag{3.31}$$

where the components considered are the gain from the left leaf, the gain from the right leaf, and the score of the original leaf.

3.C.7 Gradient Boosting Regression

Gradient boosting regression relies on the construction of many weak prediction models that is built in an iterative process. The weak models in this case, and most often are, decision trees. A simplified description is provided here. First a base estimator, $F_0(x)$, is first trained on the data:

$$F_o(x) = \arg\min_{\gamma} \sum_{i=1}^{n} L(y_i, \gamma) \tag{3.32}$$

where L is a differentiable loss function. The pseudo-residuals, r_{im}, are then calculated for every data point i:

$$r_{im} = -\left[\frac{\partial L(y_i, F(x_i))}{\partial F(x_i)}\right] \tag{3.33}$$

Another weak learner, $h_m(x)$, is then trained on the pseudo-residuals and the weight associated with the model, γ_m, is calculated using an optimization procedure. Not that here m indicates the current iteration of a total of M steps. The new model then has the form of:

$$\hat{F}(x) = \sum_{i=1}^{M} \gamma_i h_i(x) \tag{3.34}$$

New learners are then added to the model iteratively by re-calculating the pseudo-residuals to train a weak model and find it weights. This procedure can continue for an arbitrary number of steps or until a training metric passes a threshold.

3.C.8 Artificial Neural Networks

Fully dense artificial neural networks are composed of a network of many layers of interconnected nodes. Each node is connected to all nodes in the previous and following layers by a unique weight w. It is easiest to describe a neural network through the behavior of a single node - a diagram of which is provided in Figure 3.18. The output of node i in layer j is calculated as:

$$a_{ij} = \sum_{i=1}^{n} w_i x_i + b \tag{3.35}$$

where b is a node-specific constant and there are n nodes feeding into the node a_{ij}. The value that feeds to all nodes in the following layer is then calculated as $f(a_{ij})$, where f is an activation function such as tan. For a regression problem there is often a final layer with a single node with no activation function to make predictions. The weights w and constants b are initially randomized and then learned through the training process. A mathematical description of the training procedure is beyond the scope of this work. The number of layers,

activation function, and training procedure are all hyperparameters that can be optimized to best suit the problem at hand.

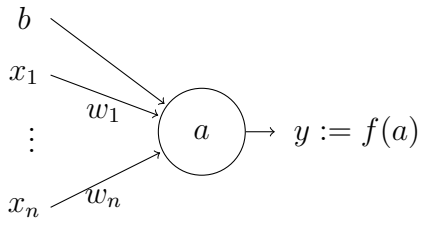

Figure 3.18: Diagram of a single neuron in a neural network.

3.D Performance of Machine Learning Models

The prediction accuracy of the various regression models can be shown by comparing the predicted output parameter versus the true input parameter for each simulation. This comparison is shown below in Figure 3.19 for multiple regression models. Each subplot shows the author-selected input parameter data in red, and the randomly selected input parameter data in blue. Each subplot also has a dotted line with slope = 1 which can be used to determine the accuracy of each point. For a given simulation, if the predicted value matched the true value of the parameter, that point would fall on the dotted line. Therefore, any points in the upper triangle of a plot have an output parameter that is over-predicted by the regression model, and any points in the lower triangle have been under-predicted by the model.

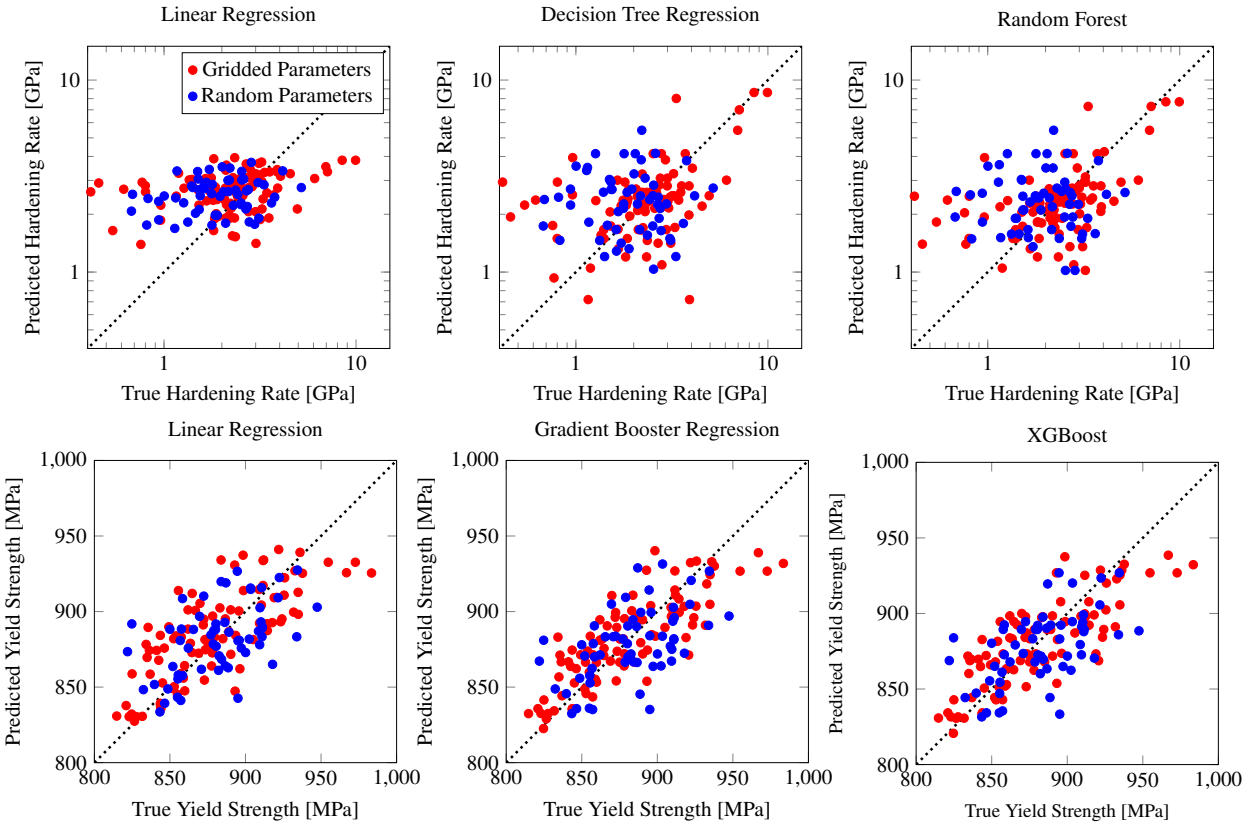

Figure 3.19: True and predicted yield strength and hardening values for the the several models using the gridded and random test sets.

CHAPTER 4

Future work

While the simulation methods described were designed for metals with well-known properties, the simulations can be easily reformulated to simulate various metals, including new materials such as high entropy alloys (HEAs). The present additive manufacturing simulation requires various material properties such as density, entropy of fusion, melting point, and others that could be readily calculated from lab-scale test samples of HEAs. The current additive manufacturing model could also be expanded to include laser parameters that were not used in this study. These parameters could include various laser powers, as well as other manufacture methods entirely like electron beam melting, or additive wire arc manufacturing. Bolstering the simulation with a wider feature set would improve the thermo-physical simulation of the input material, outputting more accurate microstructures of the final material. In consideration of the thermal portion of the model, expansion to a true 3D model would also improve the microstructural outputs by more accurately modeling the features of the melt pool and grain growth down through the bulk of the previously fused material.

While the thermo-physical phase field model is currently applicable to many materials, improvements can be made to better simulate many of the defects that appear in additive manufacturing processes. Retention of these defects throughout the microstructure would allow for more accurate finite-element simulations to better determine the expected elastic modulus, yield strength, hardening rate, and other mechanical properties.

Another potentially interesting application of this model could be used to determine the feasibility of rapid prototyping HEAs with compositional gradations. Compositionally

graded materials are well-suited for applications that require a material capable of exhibiting mechanical properties in specific localized areas. The combination of the advanced properties seen in HEAs with the complicated geometries producible with additive manufacturing methods could lead to industrial advances at reduced cost and shorter prototyping cycle times.

Bibliography

1. Liu, S., Lee, M., Choi, C. & Shin, K. Effect of additive manufacturing of SUS316L using selective laser melting. *Journal of Materials Research and Technology* **24,** 9824–9833. ISSN: 2238-7854 (May 1, 2023).

2. Liu, J., Jalalahmadi, B., Guo, Y., Sealy, M. P. & Bolander, N. A review of computational modeling in powder-based additive manufacturing for metallic part qualification. *Rapid Prototyping Journal* **24,** 1245–1264. ISSN: 1355-2546 (Nov. 14, 2018).

3. Liverani, E., Toschi, S., Ceschini, L. & Fortunato, A. Effect of selective laser melting (SLM) process parameters on microstructure and mechanical properties of 316L austenitic stainless steel. *Journal of Materials Processing Technology* **249,** 255–263. ISSN: 0924-0136 (Nov. 1, 2017).

4. Lewandowski, J. J. & Seifi, M. Metal Additive Manufacturing: A Review of Mechanical Properties. *Annual Review of Materials Research* **46.** _eprint: https://doi.org/10.1146/annurev-matsci-070115-032024, 151–186 (2016).

5. Plotkowski, A., Kirka, M. M. & Babu, S. S. Verification and validation of a rapid heat transfer calculation methodology for transient melt pool solidification conditions in powder bed metal additive manufacturing. *Additive Manufacturing* **18,** 256–268. ISSN: 2214-8604 (Dec. 1, 2017).

6. Liu, P. *et al.* Insight into the mechanisms of columnar to equiaxed grain transition during metallic additive manufacturing. *Additive Manufacturing* **26,** 22–29. ISSN: 2214-8604 (Mar. 1, 2019).

7. Sing, S. L., Wiria, F. E. & Yeong, W. Y. Selective laser melting of lattice structures: A statistical approach to manufacturability and mechanical behavior. *Robotics and Computer-Integrated Manufacturing* **49,** 170–180. ISSN: 0736-5845 (Feb. 1, 2018).

8. King, W. *et al.* Overview of modelling and simulation of metal powder bed fusion process at Lawrence Livermore National Laboratory. *Materials Science and Technology* **31,** 957–968 (2015).

9. Lee, Y. & Zhang, W. Modeling of heat transfer, fluid flow and solidification microstructure of nickel-base superalloy fabricated by laser powder bed fusion. *Additive Manufacturing* **12,** 178–188 (2016).

10. Francois, M. M. *et al.* Modeling of additive manufacturing processes for metals: Challenges and opportunities. *Current Opinion in Solid State and Materials Science* **21,** 198–206 (2017).

11. Bayat, M., Dong, W., Thorborg, J., To, A. C. & Hattel, J. H. A review of multi-scale and multi-physics simulations of metal additive manufacturing processes with focus on modeling strategies. *Additive Manufacturing* **47,** 102278 (2021).

12. Turner, J. A. *et al.* ExaAM: Metal additive manufacturing simulation at the fidelity of the microstructure. *The International Journal of High Performance Computing Applications* **36,** 13–39 (2022).

13. Gatsos, T., Elsayed, K. A., Zhai, Y. & Lados, D. A. Review on computational modeling of process–microstructure–property relationships in metal additive manufacturing. *Jom* **72,** 403–419 (2020).

14. Ji, Y., Chen, L. & Chen, L.-Q. in *Thermo-mechanical modeling of additive manufacturing* 93–116 (Elsevier, 2018).

15. Yang, M., Wang, L. & Yan, W. Phase-field modeling of grain evolutions in additive manufacturing from nucleation, growth, to coarsening. *Npj Computational Materials* **7,** 56 (2021).

16. Sahoo, S. & Chou, K. Phase-field simulation of microstructure evolution of Ti–6Al–4V in electron beam additive manufacturing process. *Additive manufacturing* **9,** 14–24 (2016).

17. Chadwick, A. F. & Voorhees, P. W. The development of grain structure during additive manufacturing. *Acta Materialia* **211,** 116862 (2021).

18. Rodgers, T. M., Madison, J. D. & Tikare, V. Simulation of metal additive manufacturing microstructures using kinetic Monte Carlo. *Computational Materials Science* **135,** 78–89 (2017).

19. Ouyang, K., Kuang, Y. & Jiang, J. Quantitative Simulation Study of Metal Additive Manufacturing by Kinetic Monte Carlo. *Journal of Applied Mathematics and Physics* **10,** 1587–1601 (2022).

20. Liu, P. *et al.* Investigation of thermal responses during metallic additive manufacturing using a "Tri-Prism" finite element method. *International Journal of Thermal Sciences* **136,** 217–229 (2019).

21. Neiva, E., Badia, S., Martıń, A. F. & Chiumenti, M. A scalable parallel finite element framework for growing geometries. Application to metal additive manufacturing. *International Journal for Numerical Methods in Engineering* **119,** 1098–1125 (2019).

22. Teferra, K. & Rowenhorst, D. J. Optimizing the cellular automata finite element model for additive manufacturing to simulate large microstructures. *Acta Materialia* **213,** 116930 (2021).

23. Yang, Q. *et al.* Finite element modeling and validation of thermomechanical behavior of Ti-6Al-4V in directed energy deposition additive manufacturing. *Additive Manufacturing* **12,** 169–177 (2016).

24. Aggarwal, A. & Kumar, A. Particle scale modelling of selective laser melting-based additive manufacturing process using open-source CFD code OpenFOAM. *Transactions of the Indian Institute of Metals* **71,** 2813–2817 (2018).

25. Liu, S. & Shin, Y. C. Integrated 2D cellular automata-phase field modeling of solidification and microstructure evolution during additive manufacturing of Ti6Al4V. *Computational Materials Science* **183,** 109889 (2020).

26. Raghavan, S. & Sahay, S. S. Modeling the grain growth kinetics by cellular automaton. *Materials Science and Engineering: A* **445,** 203–209 (2007).

27. Janssens, K. An introductory review of cellular automata modeling of moving grain boundaries in polycrystalline materials. *Mathematics and Computers in Simulation* **80,** 1361–1381 (2010).

28. Lian, Y., Lin, S., Yan, W., Liu, W. K. & Wagner, G. J. A parallelized three-dimensional cellular automaton model for grain growth during additive manufacturing. *Computational Mechanics* **61,** 543–558 (2018).

29. Mohebbi, M. S. & Ploshikhin, V. Implementation of nucleation in cellular automaton simulation of microstructural evolution during additive manufacturing of Al alloys. *Additive Manufacturing* **36,** 101726 (2020).

30. Yang, M., Wang, L. & Yan, W. Phase-field modeling of grain evolutions in additive manufacturing from nucleation, growth, to coarsening. *npj Computational Materials* **7.** Number: 1 Publisher: Nature Publishing Group, 1–12. ISSN: 2057-3960 (Apr. 28, 2021).

31. Akram, J., Chalavadi, P., Pal, D. & Stucker, B. Understanding grain evolution in additive manufacturing through modeling. *Additive Manufacturing* **21,** 255–268. ISSN: 2214-8604 (May 1, 2018).

32. Roehling, T. T. *et al.* Controlling grain nucleation and morphology by laser beam shaping in metal additive manufacturing. *Materials & Design* **195,** 109071. ISSN: 0264-1275 (Oct. 1, 2020).

33. Li, X. & Tan, W. Numerical investigation of effects of nucleation mechanisms on grain structure in metal additive manufacturing. *Computational Materials Science* **153,** 159–169. ISSN: 0927-0256 (Oct. 1, 2018).

34. Dinda, G. P., Dasgupta, A. K. & Mazumder, J. Texture control during laser deposition of nickel-based superalloy. *Scripta Materialia* **67,** 503–506. ISSN: 1359-6462 (Sept. 1, 2012).

35. Zhang, L.-C., Chen, L.-Y. & Wang, L. Surface Modification of Titanium and Titanium Alloys: Technologies, Developments, and Future Interests. *Advanced engineering materials* **22** (2020-05).

36. Eylon, D., Fujishiro, S., Postans, P. J. & Froes, F. H. High-Temperature Titanium Alloys–a Review. English. *J.Met.* **36,** 55–62 (1984).

37. Markovsky, P. E. *et al.* Effect of Strain Rate on Microstructure Evolution and Mechanical Behavior of Titanium-Based Materials. *Metals* **10,** 1404 (2020).

38. Lütjering, G. & Williams, J. C. *Titanium* (Springer Science & Business Media, 2007).

39. Thijs, L., Verhaeghe, F., Craeghs, T., Van Humbeeck, J. & Kruth, J.-P. A study of the microstructural evolution during selective laser melting of Ti–6Al–4V. *Acta materialia* **58,** 3303–3312 (2010).

40. Prikhodko, S. V., Markovsky, P. E., Savvakin, D. G., Stasiuk, O. & Ivasishin, O. M. *Thermo-mechanical treatment of titanium based layered structures fabricated by blended elemental powder metallurgy* in *Materials Science Forum* **941** (2018), 1384–1390.

41. Kawano, Y. *et al.* Crystal Plasticity Analysis of Microscopic Deformation Mechanisms and GN Dislocation Accumulation Depending on Vanadium Content in β Phase of Two-Phase Ti Alloy. *Materials Transactions* **60,** 959–968 (2019).

42. Kapoor, K. *et al.* Modeling Ti–6Al–4V using crystal plasticity, calibrated with multi-scale experiments, to understand the effect of the orientation and morphology of the α and β phases on time dependent cyclic loading. *Journal of the Mechanics and Physics of Solids* **146,** 104192 (2021).

43. Bin, T. *et al.* Crystal plasticity finite element study of incompatible deformation behavior in two phase microstructure in near β titanium alloy. *Rare Metal Materials and Engineering* **44,** 532–537 (2015).

44. Mayeur, J. & McDowell, D. A three-dimensional crystal plasticity model for duplex Ti–6Al–4V. *International journal of plasticity* **23,** 1457–1485 (2007).

45. Aubry, S., Rhee, M., Hommes, G., Bulatov, V. & Arsenlis, A. Dislocation dynamics in hexagonal close-packed crystals. *Journal of the Mechanics and Physics of Solids* **94,** 105–126 (2016).

46. Schleder, G. R., Padilha, A. C., Acosta, C. M., Costa, M. & Fazzio, A. From DFT to machine learning: recent approaches to materials science–a review. *Journal of Physics: Materials* **2,** 032001 (2019).

47. Steinberger, D., Song, H. & Sandfeld, S. Machine learning-based classification of dislocation microstructures. *Frontiers in Materials* **6,** 141 (2019).

48. Botu, V. & Ramprasad, R. Adaptive machine learning framework to accelerate ab initio molecular dynamics. *International Journal of Quantum Chemistry* **115,** 1074–1083 (2015).

49. Acar, P. Machine Learning Reinforced Crystal Plasticity Modeling under Experimental Uncertainty. *AIAA Journal* **58,** 3569–3576 (2020).

50. Mueller, T., Kusne, A. G. & Ramprasad, R. Machine learning in materials science: Recent progress and emerging applications. *Reviews in Computational Chemistry* **29,** 186–273 (2016).

51. Wei, J. *et al.* Machine learning in materials science. *InfoMat* **1,** 338–358 (2019).

52. Morgan, D. & Jacobs, R. Opportunities and challenges for machine learning in materials science. *Annual Review of Materials Research* **50,** 71–103 (2020).

53. Guo, S., Yu, J., Liu, X., Wang, C. & Jiang, Q. A predicting model for properties of steel using the industrial big data based on machine learning. *Computational Materials Science* **160,** 95–104 (2019).

54. Xiong, J., Zhang, T. & Shi, S. Machine learning of mechanical properties of steels. *Science China Technological Sciences* **63,** 1247–1255 (2020).

55. Le, T.-T. Prediction of tensile strength of polymer carbon nanotube composites using practical machine learning method. *Journal of Composite Materials* **55,** 787–811 (2021).

56. Yang, K. *et al.* Predicting the Young's modulus of silicate glasses using high-throughput molecular dynamics simulations and machine learning. *Scientific reports* **9,** 1–11 (2019).

57. Xiong, J., Zhang, T.-Y. & Shi, S.-Q. Machine learning prediction of elastic properties and glass-forming ability of bulk metallic glasses. *MRS Communications* **9,** 576–585 (2019).

58. Cai, J., Li, F., Liu, T., Chen, B. & He, M. Constitutive equations for elevated temperature flow stress of Ti–6Al–4V alloy considering the effect of strain. *Materials & Design* **32,** 1144–1151 (2011).

59. Li, X., Guo, G., Xiao, J., Song, N. & Li, D. Constitutive modeling and the effects of strain-rate and temperature on the formability of Ti–6Al–4V alloy sheet. *Materials & Design* **55,** 325–334 (2014).

60. Lee, W.-S. & Lin, C.-F. Plastic deformation and fracture behaviour of Ti–6Al–4V alloy loaded with high strain rate under various temperatures. *Materials Science and Engineering: A* **241,** 48–59 (1998).

61. Admal, N. C., Po, G. & Marian, J. Diffuse-interface polycrystal plasticity: expressing grain boundaries as geometrically necessary dislocations. *Materials Theory* **1,** 1–16 (2017).

62. Roirand, H., Malard, B., Hor, A. & Saintier, N. Effect of laser scan pattern in laser powder bed fusion process: The case of 316L stainless steel. *Procedia Structural Integrity. Fatigue Design 2021, International Conference Proceedings, 9th Edition* **38,** 149–158. ISSN: 2452-3216 (Jan. 1, 2022).

63. Todaro, C. J. *et al.* Grain structure control during metal 3D printing by high-intensity ultrasound. *Nature Communications* **11,** 142. ISSN: 2041-1723 (Jan. 9, 2020).

64. Martin, J. H. *et al.* 3D printing of high-strength aluminium alloys. *Nature* **549.** Number: 7672 Publisher: Nature Publishing Group, 365–369. ISSN: 1476-4687 (Sept. 2017).

65. Barriobero-Vila, P. *et al.* Peritectic titanium alloys for 3D printing. *Nature Communications* **9.** Number: 1 Publisher: Nature Publishing Group, 3426. ISSN: 2041-1723 (Aug. 24, 2018).

66. Xu, K., Li, B. & Jiang, C. Adjusting microstructure and improving mechanical property of additive manufacturing 316L based on process optimization. *Materials Science and Engineering: A* **870,** 144824. ISSN: 0921-5093 (Apr. 12, 2023).

67. DeWitt, S., Rudraraju, S., Montiel, D., Andrews, W. B. & Thornton, K. PRISMS-PF: A general framework for phase-field modeling with a matrix-free finite element method. *npj Computational Materials* **6,** 29 (Mar. 26, 2020).

68. Reina, C., Sandoval, L. & Marian, J. Mesoscale computational study of the nanocrystallization of amorphous Ge via a self-consistent atomistic phase-field model. *Acta Materialia* **77,** 335–351. ISSN: 1359-6454 (Sept. 15, 2014).

69. Lo, Y.-S., Borden, M. J., Ravi-Chandar, K. & Landis, C. M. A phase-field model for fatigue crack growth. *Journal of the Mechanics and Physics of Solids* **132,** 103684. ISSN: 0022-5096 (Nov. 1, 2019).

70. Yamanaka, A. Phase-field Modeling and Simulation of Solid-state Phase Transformations in Steels. *ISIJ International* **63,** 395–406 (2023).

71. Löser, W. & Herlach, D. M. Theoretical treatment of the solidification of undercooled Fe-Cr-Ni melts. *Metallurgical Transactions A* **23,** 1585–1591. ISSN: 2379-0180 (May 1, 1992).

72. Allen, S. M. & Cahn, J. W. A microscopic theory for antiphase boundary motion and its application to antiphase domain coarsening. *Acta Metallurgica* **27,** 1085–1095. ISSN: 0001-6160 (June 1, 1979).

73. Krielaart, G. P. & van der Zwaag, S. Simulations of pro-eutectoid ferrite formation using a mixed control growth model. *Materials Science and Engineering: A* **246,** 104–116. ISSN: 0921-5093 (May 15, 1998).

74. Di Schino, A., Kenny, J. M. & Abbruzzese, G. Analysis of the recrystallization and grain growth processes in AISI 316 stainless steel. *Journal of Materials Science* **37,** 5291–5298. ISSN: 1573-4803 (Dec. 1, 2002).

75. Kern, M., Bernhard, M., Bernhard, C. & Kang, Y.-B. Grain boundary mobility of γ-Fe in high-purity iron during isothermal annealing. *Scripta Materialia* **230,** 115431. ISSN: 1359-6462 (June 1, 2023).

76. Cruz-Fabiano, A. L., Logé, R. & Bernacki, M. Assessment of simplified 2D grain growth models from numerical experiments based on a level set framework. *Computational Materials Science* **92,** 305–312. ISSN: 0927-0256 (Sept. 1, 2014).

77. Kim, C. S. *Thermophysical properties of stainless steels* ANL-75-55 (Argonne National Lab., Ill. (USA), Sept. 1, 1975).

78. Pichler, P., Simonds, B. J., Sowards, J. W. & Pottlacher, G. Measurements of thermophysical properties of solid and liquid NIST SRM 316L stainless steel. *Journal of Materials Science* **55,** 4081–4093. ISSN: 1573-4803 (Mar. 1, 2020).

79. Wilthan, B., Reschab, H., Tanzer, R., Schützenhöfer, W. & Pottlacher, G. Thermophysical Properties of a Chromium–Nickel–Molybdenum Steel in the Solid and Liquid Phases. *International Journal of Thermophysics* **29,** 434–444. ISSN: 1572-9567 (Feb. 1, 2008).

80. Fletcher, N. H. Size Effect in Heterogeneous Nucleation. *The Journal of Chemical Physics* **29,** 572–576. ISSN: 0021-9606, 1089-7690 (Sept. 1, 1958).

81. Mura, E. & Ding, Y. Nucleation of melt: From fundamentals to dispersed systems. *Advances in Colloid and Interface Science* **289,** 102361. ISSN: 0001-8686 (Mar. 1, 2021).

82. Turnbull, D. & Fisher, J. C. Rate of Nucleation in Condensed Systems. *The Journal of Chemical Physics* **17,** 71–73. ISSN: 0021-9606, 1089-7690 (Jan. 1, 1949).

83. Lin, H., Ran, H., Zhong, S. & Ku, J. Review on nucleation and growth behavior of iron grain during deep reduction. *Powder Technology* **424,** 118531. ISSN: 0032-5910 (June 15, 2023).

84. Gandin, C.-A. A coupled finite element-cellular automaton model for the prediction of dendritic grain structures in solidification processes. *Acta metallurgica et materialia* **42,** 2233–2246 (1994).

85. Gandin, C.-A. Probabilistic modelling of microstructure formation in solidification processes. *Acta metallurgica et materialia* **41,** 345–360 (1993).

86. Chen, Q., Guillemot, G., Gandin, C.-A. & Bellet, M. Three-dimensional finite element thermomechanical modeling of additive manufacturing by selective laser melting for ceramic materials. *Additive Manufacturing* **16,** 124–137 (2017).

87. Penelle, R. Nucleation and growth during primary recrystallization of certain metals and alloys with a face-centered cubic structure: Formation of the cube texture. *International journal of materials research* **100,** 1420–1432 (2009).

88. Kestens, L. & Pirgazi, H. *Texture formation in metal alloys with cubic crystal structures* 2016.

89. Ishimoto, T., Hagihara, K., Hisamoto, K. & Nakano, T. Stability of crystallographic texture in laser powder bed fusion: Understanding the competition of crystal growth using a single crystalline seed. *Additive Manufacturing* **43,** 102004 (2021).

90. Li, J. N., Gao, D., Lu, Y., Hao, Z. P. & Wang, Z. Q. Mechanical properties and microstructure evolution of additive manufactured 316L stainless steel under dynamic loading. *Materials Science and Engineering: A* **855,** 143896. ISSN: 0921-5093 (Oct. 10, 2022).

91. Röttger, A. *et al.* Microstructure and mechanical properties of 316L austenitic stainless steel processed by different SLM devices. *The International Journal of Advanced Manufacturing Technology* **108,** 769–783. ISSN: 1433-3015 (May 1, 2020).

92. Saboori, A. *et al.* Microstructure and Mechanical Properties of AISI 316L Produced by Directed Energy Deposition-Based Additive Manufacturing: A Review. *Applied Sciences* **10.** Number: 9 Publisher: Multidisciplinary Digital Publishing Institute, 3310. ISSN: 2076-3417 (Jan. 2020).

93. Chen, X. *et al.* Microstructure and mechanical properties of the austenitic stainless steel 316L fabricated by gas metal arc additive manufacturing. *Materials Science and Engineering: A* **703,** 567–577. ISSN: 0921-5093 (Aug. 4, 2017).

94. Murr, L. Metallurgy of additive manufacturing: Examples from electron beam melting. *Additive Manufacturing* **5,** 40–53 (2015).

95. DebRoy, T. *et al.* Additive manufacturing of metallic components–process, structure and properties. *Progress in Materials Science* **92,** 112–224 (2018).

96. Megahed, S. *et al.* Manufacturing of Pure Copper with Electron Beam Melting and the Effect of Thermal and Abrasive Post-Processing on Microstructure and Electric Conductivity. *Materials* **16,** 73 (2022).

97. Haghdadi, N., Laleh, M., Moyle, M. & Primig, S. Additive manufacturing of steels: a review of achievements and challenges. *Journal of Materials Science* **56,** 64–107 (2021).

98. Balbaa, M. *et al.* Role of powder particle size on laser powder bed fusion processability of AlSi10mg alloy. *Additive manufacturing* **37,** 101630 (2021).

99. Shoji Aota, L., Bajaj, P., Zschommler Sandim, H. R. & Aimé Jägle, E. Laser powder-bed fusion as an alloy development tool: Parameter selection for in-situ alloying using elemental powders. *Materials* **13,** 3922 (2020).

100. Habiba, U. & Hebert, R. J. Powder Spreading Mechanism in Laser Powder Bed Fusion Additive Manufacturing: Experiments and Computational Approach Using Discrete Element Method. *Materials* **16,** 2824 (2023).

101. Niendorf, T. *et al.* Highly anisotropic steel processed by selective laser melting. *Metallurgical and materials transactions B* **44,** 794–796 (2013).

102. Qi, X., Takata, N., Suzuki, A., Kobashi, M. & Kato, M. Laser powder bed fusion of a near-eutectic Al–Fe binary alloy: Processing and microstructure. *Additive Manufacturing* **35,** 101308 (2020).

103. Li, R., Liu, J., Shi, Y., Du, M. & Xie, Z. 316L Stainless Steel with Gradient Porosity Fabricated by Selective Laser Melting. *Journal of Materials Engineering and Performance* **19,** 666–671. ISSN: 1059-9495, 1544-1024 (July 2010).

104. Wang, L., Zhang, Y., Chia, H. Y. & Yan, W. Mechanism of keyhole pore formation in metal additive manufacturing. *npj Computational Materials* **8.** Number: 1 Publisher: Nature Publishing Group, 1–11. ISSN: 2057-3960 (Jan. 27, 2022).

105. Kononenko, D. Y., Nikonova, V., Seleznev, M., van den Brink, J. & Chernyavsky, D. An in situ crack detection approach in additive manufacturing based on acoustic emission and machine learning. *Additive Manufacturing Letters* **5,** 100130. ISSN: 2772-3690 (Apr. 1, 2023).

106. Ghayoomi Mohammadi, M., Mahmoud, D. & Elbestawi, M. On the application of machine learning for defect detection in L-PBF additive manufacturing. *Optics & Laser Technology* **143,** 107338. ISSN: 0030-3992 (Nov. 1, 2021).

107. Zöller, C., Adams, N. A. & Adami, S. Numerical investigation of balling defects in laser-based powder bed fusion of metals with Inconel 718. *Additive Manufacturing* **73,** 103658. ISSN: 2214-8604 (July 5, 2023).

108. Lindström, V., Lupo, G., Yang, J., Turlo, V. & Leinenbach, C. A simple scaling model for balling defect formation during laser powder bed fusion. *Additive Manufacturing* **63,** 103431. ISSN: 2214-8604 (Feb. 5, 2023).

109. Mukherjee, T. & DebRoy, T. Mitigation of lack of fusion defects in powder bed fusion additive manufacturing. *Journal of Manufacturing Processes* **36,** 442–449. ISSN: 1526-6125 (Dec. 1, 2018).

110. Darvish, K., Chen, Z. W. & Pasang, T. Reducing lack of fusion during selective laser melting of CoCrMo alloy: Effect of laser power on geometrical features of tracks. *Materials & Design* **112,** 357–366. ISSN: 0264-1275 (Dec. 15, 2016).

111. Bauereiß, A., Scharowsky, T. & Körner, C. Defect generation and propagation mechanism during additive manufacturing by selective beam melting. *Journal of Materials Processing Technology* **214,** 2522–2528. ISSN: 0924-0136 (Nov. 1, 2014).

112. Barton, N. R., Arsenlis, A. & Marian, J. A polycrystal plasticity model of strain localization in irradiated iron. *Journal of the Mechanics and Physics of Solids* **61,** 341–351 (2013).

113. Moore, J. A., Barton, N. R., Florando, J., Mulay, R. & Kumar, M. Crystal plasticity modeling of β phase deformation in Ti-6Al-4V. *Modelling and Simulation in Materials Science and Engineering* **25,** 075007 (2017).

114. Fundenberger, J., Philippe, M., Wagner, F. & Esling, C. Modelling and prediction of mechanical properties for materials with hexagonal symmetry (zinc, titanium and zirconium alloys). *Acta materialia* **45,** 4041–4055 (1997).

115. Semiatin, S. & Bieler, T. Effect of texture and slip mode on the anisotropy of plastic flow and flow softening during hot working of Ti-6Al-4V. *Metallurgical and Materials Transactions A* **32,** 1787–1799 (2001).

116. Paton, N. The deformation of α-phase titanium. *Titanium science and technology* (1973).

117. Babu, B. & Lindgren, L.-E. Dislocation density based model for plastic deformation and globularization of Ti-6Al-4V. *International Journal of Plasticity* **50,** 94–108 (2013).

118. Chong, Y., Bhattacharjee, T., Park, M.-H., Shibata, A. & Tsuji, N. Factors determining room temperature mechanical properties of bimodal microstructures in Ti-6Al-4V alloy. *Materials Science and Engineering: A* **730,** 217–222 (2018).

119. Tanaka, Y., Hattori, K. & Harada, Y. Micro-cantilever testing of microstructural effects on plastic behavior of Ti–6Al–4V alloy. *Materials Science and Engineering: A* **823,** 141747 (2021).

120. Hémery, S., Villechaise, P. & Banerjee, D. Microplasticity at room temperature in α/β titanium alloys. *Metallurgical and Materials Transactions A* **51,** 4931–4969 (2020).

121. Stapleton, A. M. *et al.* Evolution of lattice strain in Ti-6Al-4V during tensile loading at room temperature. *Acta Materialia* **56,** 6186–6196 (2008).

122. Venkatesh, B., Chen, D. & Bhole, S. Effect of heat treatment on mechanical properties of Ti–6Al–4V ELI alloy. *Materials Science and Engineering: A* **506,** 117–124 (2009).

123. Hu, H., Xu, Z., Dou, W. & Huang, F. Effects of strain rate and stress state on mechanical properties of Ti-6Al-4V alloy. *International Journal of Impact Engineering* **145,** 1 (Nov. 2020).

124. Song, K., Yan, F., Ding, T., Gao, L. & Lu, S. A steel property optimization model based on the XGBoost algorithm and improved PSO. *Computational Materials Science* **174,** 109472 (2020).

125. Bhagat, S. K., Tiyasha, T., Tung, T. M., Mostafa, R. R. & Yaseen, Z. M. Manganese (Mn) removal prediction using extreme gradient model. *Ecotoxicology and Environmental Safety* **204,** 111059 (2020).

126. Dong, G. *et al.* Machine learning guided methods in building chemical composition-hardenability model for wear-resistant steel. *Materials Today Communications* **24,** 101332 (2020).

127. Friedman, J., Hastie, T., Tibshirani, R., *et al. The elements of statistical learning* **10** (Springer series in statistics New York, 2001).

128. Breiman, L. Random forests. *Machine learning* **45,** 5–32 (2001).

129. Svetnik, V. *et al.* Random forest: a classification and regression tool for compound classification and QSAR modeling. *Journal of chemical information and computer sciences* **43,** 1947–1958 (2003).

130. Chen, T. & Guestrin, C. *Xgboost: A scalable tree boosting system* in *Proceedings of the 22nd acm sigkdd international conference on knowledge discovery and data mining* (2016), 785–794.

131. Friedman, J. H. Greedy function approximation: a gradient boosting machine. *Annals of statistics,* 1189–1232 (2001).

132. Friedman, J., Hastie, T. & Tibshirani, R. Additive logistic regression: a statistical view of boosting (with discussion and a rejoinder by the authors). *The annals of statistics* **28,** 337–407 (2000).

133. Friedman, J. H. Stochastic gradient boosting. *Computational statistics & data analysis* **38,** 367–378 (2002).

134. Zurada, J. M. *Introduction to artificial neural systems* (West St. Paul, 1992).

135. Hkdh, B. Neural networks in materials science. *ISIJ international* **39,** 966–979 (1999).

136. Pedregosa, F. *et al.* Scikit-learn: Machine learning in Python. *the Journal of machine Learning research* **12,** 2825–2830 (2011).

137. Caruana, R. & Niculescu-Mizil, A. *An empirical comparison of supervised learning algorithms* in *Proceedings of the 23rd international conference on Machine learning* (2006), 161–168.

138. Strobl, C., Boulesteix, A.-L., Zeileis, A. & Hothorn, T. Bias in random forest variable importance measures: Illustrations, sources and a solution. *BMC bioinformatics* **8,** 1–21 (2007).

139. Kaufmann, K. *et al.* Discovery of high-entropy ceramics via machine learning. *Npj Computational Materials* **6,** 1–9 (2020).

140. Mangal, A. & Holm, E. A. A comparative study of feature selection methods for stress hotspot classification in materials. *Integrating Materials and Manufacturing Innovation* **7,** 87–95 (2018).

141. Anysz, H., Brzozowski, Ł., Kretowicz, W. & Narloch, P. Feature importance of stabilised rammed earth components affecting the compressive strength calculated with explainable artificial intelligence tools. *Materials* **13,** 2317 (2020).

142. Wu, C.-T. *et al.* Machine learning recommends affordable new Ti alloy with bone-like modulus. *Materials Today* **34,** 41–50 (2020).

143. Zhu, C. *et al.* A titanium alloys design method based on high-throughput experiments and machine learning. *Journal of Materials Research and Technology* **11,** 2336–2353 (2021).

144. Johnson, A. W., Bull, C., Kumar, K. & Briant, C. The influence of microstructure and strain rate on the compressive deformation behavior of Ti-6Al-4V. *Metallurgical and Materials Transactions A* **34,** 295–306 (2003).

145. Ren, Y., Zhou, S., Luo, W., Xue, Z. & Zhang, Y. *Influence of primary α-phase volume fraction on the mechanical properties of Ti-6Al-4V alloy at different strain rates and temperatures* in *IOP Conference Series: Materials Science and Engineering* **322** (2018), 022022.

146. Wang, S., Liu, J. & Chen, D. Effect of strain rate and temperature on strain hardening behavior of a dissimilar joint between Ti–6Al–4V and Ti17 alloys. *Materials & Design (1980-2015)* **56,** 174–184 (2014).

147. Park, C. H., Son, Y. I. & Lee, C. S. Constitutive analysis of compressive deformation behavior of ELI-grade Ti–6Al–4V with different microstructures. *Journal of Materials Science* **47,** 3115–3124 (2012).

148. Follansbee, P. & Gray, G. An analysis of the low temperature, low and high strain-rate deformation of Ti- 6Al- 4V. *Metallurgical Transactions A* **20,** 863–874 (1989).

149. Tabei, A., Abed, F., Voyiadjis, G. & Garmestani, H. Constitutive modeling of Ti-6Al-4V at a wide range of temperatures and strain rates. *European Journal of Mechanics-A/Solids* **63,** 128–135 (2017).

150. Khan, A. S., Yu, S. & Liu, H. Deformation induced anisotropic responses of Ti–6Al–4V alloy Part II: A strain rate and temperature dependent anisotropic yield criterion. *International Journal of Plasticity* **38,** 14–26 (2012).

151. Guan, R. G., Je, Y. T., Zhao, Z. Y. & Lee, C. S. Effect of microstructure on deformation behavior of Ti–6Al–4V alloy during compressing process. *Materials & Design (1980-2015)* **36,** 796–803 (2012).

152. Ren, Y. *et al. Effect of α-platelet thickness on the mechanical properties of Ti-6Al-4V alloy with lamellar microstructure* in *IOP Conference Series: Materials Science and Engineering* **281** (2017), 012024.

153. Wu, G., Shi, C., Sha, W., Sha, A. & Jiang, H. Effect of microstructure on the fatigue properties of Ti–6Al–4V titanium alloys. *Materials & Design* **46,** 668–674 (2013).

154. Zhang, X.-Y. *et al.* Effect of subtransus heat treatment on the microstructure and mechanical properties of additively manufactured Ti-6Al-4V alloy. *Journal of Alloys and Compounds* **735,** 1562–1575 (2018).

155. Obasi, G., Ferri, O., Ebel, T. & Bormann, R. Influence of processing parameters on mechanical properties of Ti–6Al–4V alloy fabricated by MIM. *Materials Science and Engineering: A* **527,** 3929–3935 (2010).

156. Lee, D.-G., Lee, S., Lee, C. S. & Hur, S. Effects of microstructural factors on quasi-static and dynamic deformation behaviors of Ti-6Al-4V alloys with widmanstätten structures. *Metallurgical and Materials Transactions A* **34,** 2541–2548 (2003).

157. Senkov, O., Valencia, J., Senkova, S., Cavusoglu, M. & Froes, F. Effect of cooling rate on microstructure of Ti-6Al-4V forging. *Materials science and technology* **18,** 1471–1478 (2002).

158. Sen, I., Tamirisakandala, S., Miracle, D. & Ramamurty, U. Microstructural effects on the mechanical behavior of B-modified Ti–6Al–4V alloys. *Acta Materialia* **55,** 4983–4993 (2007).

159. Bühlmann, P. in *Handbook of computational statistics* 985–1022 (Springer, 2012).

160. Marker, C., Shang, S.-L., Zhao, J.-C. & Liu, Z.-K. Effects of alloying elements on the elastic properties of bcc Ti-X alloys from first-principles calculations. *Computational Materials Science* **142,** 215–226 (2018).

161. Ledbetter, H., Ogi, H., Kai, S., Kim, S. & Hirao, M. Elastic constants of body-centered-cubic titanium monocrystals. *Journal of Applied Physics* **95,** 4642–4644 (2004).

162. Tromans, D. Elastic Anisotropy of HCP Metal Crystals and Polycrystals. *Int. J. Res. Rev. Appl. Sci.* **6** (Jan. 2011).

163. Frank, F. C. On Miller–Bravais indices and four-dimensional vectors. *Acta Crystallographica* **18,** 862–866 (May 1965).

164. Cereceda, D. *et al.* Unraveling the temperature dependence of the yield strength in single-crystal tungsten using atomistically-informed crystal plasticity calculations. *International Journal of Plasticity* **78,** 242–265 (2016).

165. Yu, Q., Martinez, E., Segurado, J. & Marian, J. A stochastic solver based on the residence time algorithm for crystal plasticity models. *Computational Mechanics,* 1–16 (2021).